Aeroacoustics of sawtooth trailing-edge serrations under aerodynamic loading

(Article begins on next page)

02 May 2024

Aeroacoustics of sawtooth trailing-edge serrations under aerodynamic loading

Lourenco T. Lima Pereira [*], Daniele Ragni, Francesco Avallone, Fulvio Scarano

Faculty of Aerospace Engineering, TU Delft, Kluyverweg 1, 2629HS, the Netherlands

ARTICLE INFO

ABSTRACT

The impact of aerodynamic loading on a serrated trailing edge is studied experimentally. Aerodynamic and acoustic measurements are conducted on a sawtooth-shaped trailing edge, retrofitted to a flat plate featuring a trailing-edge flap, and placed at incidence to the free-stream flow. The turbulent flow across the trailing edge is inspected by time-resolved three-dimensional velocity field measurements obtained from 4D-PIV, while the wall-pressure fluctuations are measured with surface-embedded microphones. Results discuss the relation between the velocity fluctuations over the serrations, the surface pressure fluctuations, and the far-field noise spectra. The aerodynamic analysis discusses the effect of counter-rotating vortex pairs, generated by the pressure imbalance across the edges of the serrations under loading. It is shown that the interaction of these vortices with the incoming turbulence affects the intensity of the wall-pressure spectrum at the outer rim of the serration surface. On the suction side, the intensity of the pressure fluctuations from the incoming boundary layer dominates over that induced by the vortex pairs. On the pressure side, instead, the velocity gradient prescribed by the vortex pairs produces a significant increase of the pressure fluctuations around the edges. The resulting spatial distribution of the wall-pressure fluctuations directly affects the far-field noise. Scattering predictions carried out with the wall-pressure fluctuations in the centre and root (on the suction side) exhibit good agreement with the measured noise in the low-frequency range, whereas using the surface pressure data at the tip of the serration (on the pressure side) yields a better prediction in the high-frequency range.

Introduction

Wind turbine noise is dominated by the scattering of pressure fluctuations beneath a turbulent boundary layer at the blade trailing edge [1]. This noise source, generally referred to as "turbulent boundary layer trailing-edge noise" is an efficient mechanism in generating aerodynamic noise at relatively low speeds [2]. Trailing-edge noise can be significantly reduced with trailing-edge serrations [3,4], which alter the scattering efficiency of the turbulent pressure fluctuations travelling across the slanted edge. The consensus about the effectiveness of a serrated trailing edge is demonstrated by their application in industrial wind turbines, where noise reductions of approximately 3 dB have been reported [5].

Analytical models for serrated trailing edges were first proposed by Howe [3,6], who used a compact Green's function formulation to estimate the noise reduction of serrations. This model qualitatively explains the noise reduction of trailing-edge add-ons. However,

---

* Corresponding author.
  E-mail address: L.T.LimaPereira@tudelft.nl (L.T. Lima Pereira).

acoustic measurements [7,8] systematically report a lower noise reduction. The discrepancies have been addressed in more recent works [9,10], who have provided a solution for the acoustic scattering problem on a serrated trailing edge, yielding predictions in better agreement with the experimental observations. These analytical formulations rely on the description of the aerodynamic pressure fluctuations in the wavenumber-frequency domain and make use of the frozen turbulence hypothesis [11]. As a consequence, the pressure fluctuations at the trailing edge can be inferred from the properties of the incoming turbulent boundary layer, in which the shear along the wall-normal direction is the most relevant term [12]. Sanjosé et al. [13] have recently demonstrated that the scattering model of Lyu and Ayton [14] yields the most accurate prediction of the noise reduction from a serrated trailing edge when compared to Howe's initial model.

Optimization attempts from Kholodov and Moreau [15,16] using Ayton's model have reached maximum noise reduction using slender serrations, i.e. maximum allowed (streamwise) height ($2h$) and minimum (spanwise) wavelength (λ). This trend is demonstrated in the experimental work of Gruber et al. [8]. However, the measured values of the noise reduction for slender sawtooth trailing edges [8,17] have never reached the predicted ones [14]. The discrepancies between predicted and observed noise reduction are ascribed to the mismatch between the modelled and the actual behaviour of the turbulent flow past the serrations [18]. Therefore, studies have focused on determining the unsteady flow and the inherent pressure fluctuations on the surface of the serrations with high spatial and temporal resolution. For this purpose, CFD/CAA simulations [13,19,20] and dedicated experiments [7,21] have been performed to understand the changes of flow topology over the serrated trailing edges.

When serrations are subjected to aerodynamic loading, i.e. the serrations are put at an angle with respect to the flow direction and a pressure difference exists between the upper and lower serration surface, the noise reduction is modified and references point to a degradation of the noise reduction [7,22]. Studies have examined the specific effect of the aerodynamic loading produced at the trailing-edge serrations as a consequence of the misalignment to the incoming flow direction [8,17,22]. As a result of the pressure unbalance across the slanted edges of the serration, pairs of counter-rotating trailing vortices are formed that significantly distort the streamline pattern and affect the intensity of the surface pressure fluctuations and the acoustic scattering efficiency. Arce León et al. [7] investigated, with PIV measurements, the changes in the mean-flow direction along the serration under loading and its influence on the trailing-edge noise. The study concluded that simply considering the sideward deviation of the streamlines in relation to the serration edge in the formulation of Howe [6] cannot justify the measured differences in noise reduction. The same study ascribed the degradation of noise reduction to the increase of velocity fluctuations across the span, induced by the edge vortices. Arce León et al. [17] further observed a consistent increase in the wall-normal velocity fluctuations along the pressure side of the serration at the range of frequency of noise increase for aerodynamic loaded serrations. The PIV measurements alone, however, did not enable translating the behaviour of the velocity fluctuations into the more relevant surface pressure fluctuations. To that end, a characterisation of the pressure fluctuations in relation to the three-dimensional flow behaviour is not yet available for the serrated trailing edge under aerodynamic loading and the latter is fundamental to the improvement of noise prediction models.

Obtaining accurate measurements of the surface pressure fluctuations with sufficiently high temporal and spatial resolution remains a challenging task, especially considering the thin and sharp geometry of serrations. This required resolution is, at present, at the limit of applicability of the state-of-the-art PIV techniques [23]. As a consequence, most experimental works on serrations rely upon high-frequency sampling at discrete points by hot-wire measurements [8,24] or by surface-mounted microphones, where the turbulent boundary layer only flows over one side of the serrated edge [18]. The latter approach becomes problematic for the study of serrated trailing edges at incidence, where both sides of the edge need to be exposed to the undisturbed boundary-layer turbulence.

In this work, the use of miniaturized microphones, similar to the approach of Sanders et al. [25], allows overcoming some of the above limitations. The miniature flush-mounted microphones installed along the serration surface provide spatio-temporal data of the wall-pressure fluctuations. The aerodynamic analysis instead, makes use of the recently developed large-scale 3D-PIV technique, based on Helium Filled Soap Bubbles particles [26] and time-resolved particle motion analysis by the Shake-the-Box image processing [27]. Furthermore, a data assimilation technique based on the vorticity transport equation (VIC+, Schneiders and Scarano [28]) is used to translate the measured particle trajectories into a dense velocity field and enable the pressure field reconstruction at a larger scale [29]. The combination of these measurement techniques allows visualising the large-scale velocity field distortions, caused by serrations under loading and connect them to the wall-pressure fluctuations measured by the miniaturised microphones. The experiments are complemented with far-field noise measurements that make use of microphone array techniques.

The article presents the experimental setup and the data reduction techniques in Section 2. Section 3 summarizes the existing analytical models and introduces the most relevant parameters analysed in the remainder of the paper. Section 4.1 describes the acoustic and aerodynamic properties of trailing-edge serrations under loading, while the distribution of the pressure fluctuations over the serration surface is presented in Section 4.2. A link between the mean-flow properties and the wall-pressure field is established in Section 4.3 by studying the variations of the mean shear and turbulence interaction term along the vortex core. The noise reduction obtained in comparison to the straight trailing edge is discussed in Section 4.4.

Experimental setup and methodology

Wind tunnels, model and flow conditions

Experiments are conducted in two low-speed wind tunnels of the Aerospace Engineering laboratories at TU Delft. Time-resolved 3D-PIV measurements are carried out in the W-tunnel, where a HFSB seeding particle generator is installed in the settling chamber. With the seeding generator installed, the free-stream normalised turbulence intensity is verified to be within 0.6% of the free-stream velocity. Wall pressure and acoustic measurements are instead performed in the anechoic A-tunnel (free-stream turbulence < 0.1%,

3
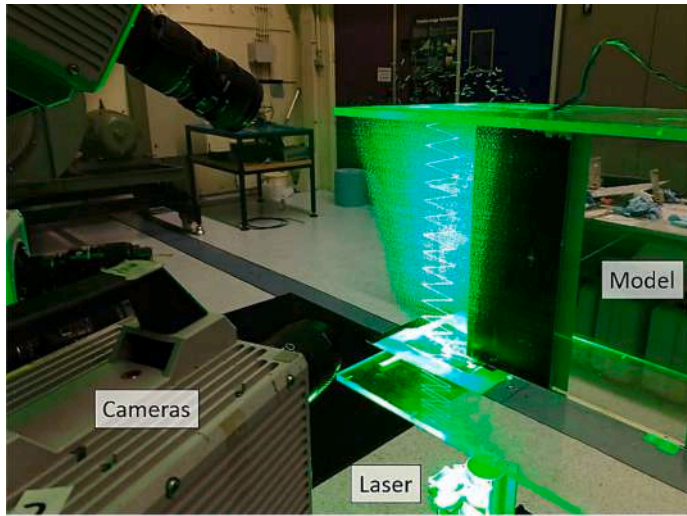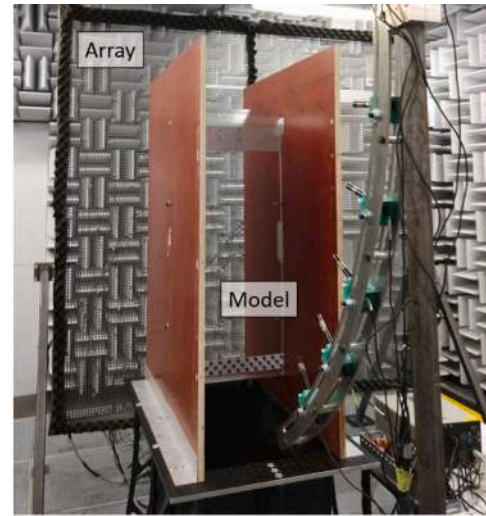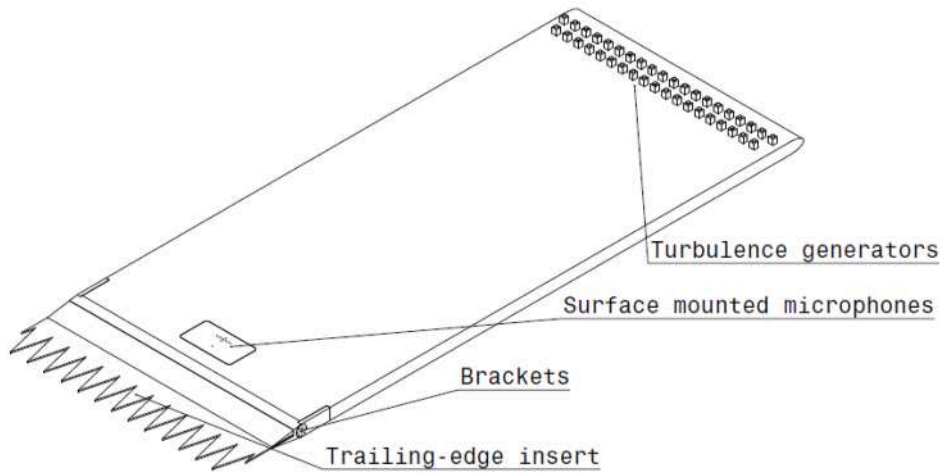
Fig. 1. Experimental set-up for the 3D-PIV (a) and acoustic (b) measurements. Details of the flat plate model (c) and the trailing-edge geometries tested (d). In the last picture, Ref. refers to the position of the baseline straight trailing edge at $X = 1h$ used. The same picture also shows the coordinate system and origin adopted in the remainder of the study.
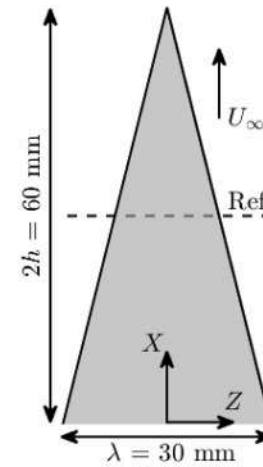
Table 1
Mean boundary-layer parameters measured at $X/2h = 0.5$ with the straight trailing-edge insert.

Parameter	Symbol	$\delta_f = 0°$	$\delta_f = 10°$ – suction side	$\delta_f = 10°$ – pressure side
Edge velocity	U_e [m/s]	10.5	11.0	9.4
Boundary-layer thickness	δ[mm]	57	60	53
Boundary-layer displacement thickness	δ^* [mm]	9.3	10.7	6.6
Boundary-layer momentum thickness	θ [mm]	6.7	7.4	5.1
Reynolds number	Re_{c^*}	670,000		
	Re_{δ^*}	6,600	7,900	4,300
Shape factor	$H = \delta^*/\theta$	1.39	1.44	1.29
Friction velocity	u_τ [m/s]	0.42	0.44	0.41
Zagarola & Smits' parameter	$\Delta_* = \delta/\delta^*$	6.1	5.5	8.0
Wake parameter	Π_w	0.36	0.52	0.11
Pressure gradient	dP/dx [Pa/m]	-8.5	45.8	-53.9
Clauser's parameter	$\beta_\theta = \left(\dfrac{\theta}{\tau_w}\right)\dfrac{dP}{dx}$	-0.27 (ZPG)	1.45 (APG)	-1.36 (FPG)

[30]). Hot-wire measurements are further carried out in the A-tunnel for verifying that the turbulent boundary layer develops with similar characteristics in both facilities.

A flat-plate model with a trailing-edge flap insert is used. The flat plate allows for the development of a turbulent boundary layer at moderate Reynolds number, and the trailing-edge flap is used to control the aerodynamic loading at the trailing-edge region. The Plexiglas flat-plate model features an elliptical leading edge. The model has 0.4 m span, 1.0 m chord, and 20 mm thickness. Boundary-layer transition is forced after the leading edge with two staggered rows of obstacles of 10 mm height and 30 mm pitch. The thick transition device follows the work of [31] and are meant to induce a thick boundary layer (approximately 60 mm height) at the measurement region. At the model end, the thickness reduces through a symmetric wedge (8° half-deflection) providing the transition to a 2 mm thickness trailing-edge insert made of Plexiglas. The edge thickness complies with the limit suggested by Blake [32] of t/δ^* < 0.3 that avoids the onset of a vortex shedding regime. The choice of a transparent material is important because it allows optical access (for PIV) on both sides of the trailing edge. The trailing-edge flap consists of a pivot (150 mm apart from the trailing edge) and two side brackets to control the flap angle (δ_f) within +/-15° by 2.5° steps. The model is installed between side plates as shown in Fig. 1. The serration height ($2h = 1\delta = 60$ mm) is selected to produce noticeable noise reduction and to permit the PIV measurements at a desirable spatial resolution. Following previous works [21], the serration wavelength is equal to half of its height ($\lambda = 30$ mm).

Experiments are performed at a free-stream velocity of 10 m/s. The incoming boundary-layer conditions, measured with PIV at $\delta_f = 0°$ and $\delta_f = 10°$, are summarized in Table 1. The velocity profile within the boundary layer presented in Table 1 is here extracted from the PIV measurements. The correct wall position (within ± 0.5 mm of the reference one) and friction velocity (u_τ) are estimated from the fit of the velocity profile with the logarithmic law of the wall [33], considering $\chi = 0.41$ and $C^+ = 5$. Integral quantities, displacement (δ^*), and momentum thickness (θ) are then computed. The law of the wake and the wake parameters (Π_w) are obtained from the formulation proposed by Coles [34]. The pressure gradient is estimated from the edge velocities (U_e) obtained at the location where the variation of the spanwise vorticity in the wall-normal direction becomes negligible, following the procedure adopted in [7] (based on the work of Spalart and Watmuff [35]). A full description of the procedures followed to estimate the boundary-layer properties at those angles along with the characterization of the incoming wall-pressure spectrum and far-field noise of the straight trailing edge is provided in Appendix A.

It is important to mention that flow separation is not observed on the suction side for any of the conditions tested. This is also verified with flow visualization techniques in both wind-tunnel facilities used.

The different inlet heights between the two facilities used (0.4 m at the W-Tunnel and 0.7 m at the A-Tunnel) can lead to small discrepancies in the induced angle due to the deflection of the jet flow. Estimations using thin airfoil theory and the corrections of Brooks et al [36] result in discrepancies below $2°$ for $\delta_f = 15°$.

Time-resolved 3D-PIV

Time-resolved volumetric PIV (4D-PIV) is performed for the flap angles of $\delta_f = 0°$, and 10° using HFSB [37] as seeding particles. The HFSB seeding system at TU Delft features 206 nozzles installed on 11 rakes aligned vertically and covering a cross-section of 1.0 m x 0.5 m, which yields a particle density of about 2 particles per cubic centimetre in the free stream. The tracers have a mean diameter of 0.4 mm and a time response of about 20 μs [26]. Illumination is provided by a high-speed Quantronix *Darwin Duo* laser (2 × 25 mJ per pulse at 1 kHz). The laser beam enters the measurement domain from the spanwise direction (Fig. 1a) expanding in both directions. The domain of illumination is truncated making use of a knife-edge filter along the wall-normal direction to a height of approximately 100 mm on each side of the model (twice the expected boundary-layer thickness) avoiding light scattering from particles outside of this range. Imaging is provided by three CMOS Photron *FASTCAM SA1.1* cameras (12 bits, 1,024 × 1,024 pixels at 5,400 fps). The cameras are placed along the streamwise direction subtending an arc of 40° at approximately 1 m distance from the trailing edge. Each camera is equipped with a 105 mm focal length objective, resulting in a field of view of about 80 mm along the streamwise and the spanwise directions. The range in the wall-normal direction is determined by the illumination and depth of focus of the imaging system and is approximately 60 mm on each side of the trailing edge. Illumination, imaging, and acquisition are synchronised with a LaVision

Table 2
Summary of PIV measurement parameters for the flow around the trailing-edge region.

| Parameter	Units	Value
Particle size	mm	0.4
Particle concentration	#/cm^3	2.5
Digital imaging resolution	px/mm (px/ δ)	10.2 (610)
Numerical aperture		f/32
Recording rate	Hz	5,400
Number of images recorded		5,400
Measured volume (X $\times$ Y $\times$ Z)	cm^3	7 $\times$ 10 $\times$ 7
	δ^3	1.2 $\times$ 1.7 $\times$ 1.2
Maximum particle displacement	px (mm)	21 (2)
VIC+ velocity vector grid spacing	mm (δ)	2.5 (4%)
Uncertainty in velocity measurements	m/s (U_∞)	0.04 (0.4%)
Uncertainty in pressure measurement	Pa	0.3
Uncertainty in the convection velocity	m/s (u_c)	0.3 (5%)
Uncertainty in the MS-T terms	Pa/m^2 ($\rho U_\infty^2/\delta^{*2}$)	1,700 (0.001)
Frequency limit*	Hz (U_∞/δ^*)	1,000 (1.0)

* based on the resolved wavenumbers
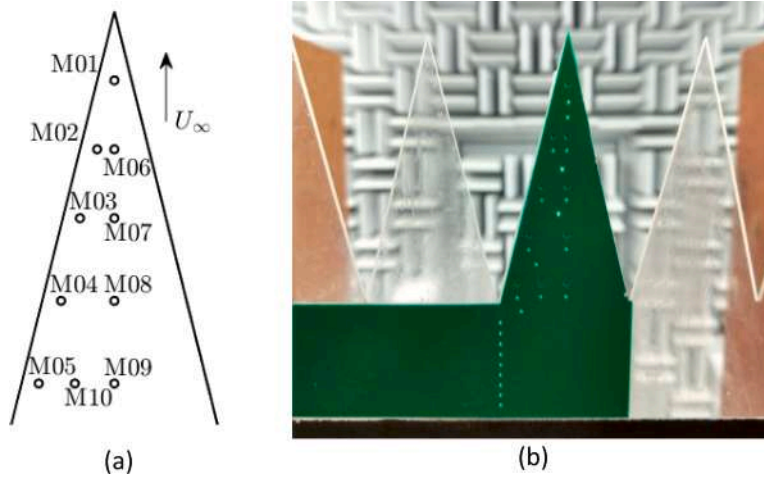
Fig. 2. Schematic description of the surface pressure sensors on the trailing-edge sawtooth (a). Photograph of the PCB integrated with the trailing-edge insert (b).

Programmable Timing Unit (*PTU 9*) controlled by LaVision *DaVis 10* software.

Images of the tracers are recorded at 5,400 frames per second. The trajectory of each tracer is evaluated with the Lagrangian Particle Tracking algorithm Shake-The-Box [27] from *DaVis 10*. The velocity measured along the particle's track is reduced to a regular Cartesian grid by data assimilation using the VIC+ technique [28]. The technique also estimates the velocity gradient and its temporal derivative, needed in the remainder of the analyses.

The instantaneous flow pressure is reconstructed in the three-dimensional domain solving the inviscid Poisson equation for pressure. The source term of the Poisson equation is computed with a Lagrangian approach using a stencil of 5 points in time, as described in Ghaemi et al. [38]. Pressure from PIV is used to estimate the convection velocity and correlation length with a higher spatial resolution than that available from the surface pressure sensors, mainly for the characterization and verification of the incoming TBL conditions. Details are given in Appendix A.

The main parameter governing the spatial resolution of the PIV measurements with HSFBs is the average distance between neighbouring particles. The latter dictates the spatial resolution through the VIC+ grid spacing one-quarter criterion [28] (velocity field reconstructed on a Cartesian mesh with vector spacing no smaller than ¼ of the average particle distance). In the present case, given the varying particle density inside the measurement volume, a more conservative choice of the grid spacing ($\Delta x = 2.5$ mm), approximately one-third of the particle mean distance, is made. The grid spacing defines the maximum wavenumber that can be resolved, in turn also limiting the maximum resolved frequency to about 1,000 Hz according to eq. (1), where u_c is the convection velocity and the constant 0.4 is a function of the VIC+ interpolation scheme. The uncertainty of the velocity measured from a single particle track depends on the particle position error (here taken as the distance between glare points of the same particle), the number of exposures composing a trajectory, and the time separation between frames. When a polynomial regression is applied to describe the particle positions in time (track), neglecting truncation errors, the velocity random error follows eq. (2) [39], where d_b represents the

Table 3
Summary of the parameters of the microphones used for the wall-pressure measurement over the serration surface.

Parameter	Units	Value
Average sensitivity	mV/Pa	18.2
Frequency limit	Hz (U_∞/δ^*)	5,000 (5)
Uncertainty in pressure measurement	Pa (dB)	0.02 (0.5)
Uncertainty in the convection velocity	m/s (u_c)	0.1 (2%)
Uncertainty in the correlation length	mm (δ)	2 (3.4%)

bubble diameter (the glare points distance is approximately $d_b/\sqrt{2}$), N the number of exposures considered by the polynomial stencil, and Δt the time separation between subsequent frames. For this experiment, a 2$^\text{nd}$ order polynomial obtained from a 9-time-step stencil yields an estimate of the instantaneous velocity uncertainty of about 0.04 m/s (0.4% of free-stream).

$$f_{VIC+} \approx 0.4 \frac{u_c}{\Delta x} \tag{1}$$

$$\varepsilon_u = \frac{d_b/\sqrt{2}}{\Delta t} N^{-3/2} \tag{2}$$

The procedure to estimate the measurement uncertainty for the instantaneous pressure is explained in Lima Pereira et al. [29]. The uncertainty on the estimations of the mean-shear turbulence (MS-T, [40]) interaction term, discussed in this work, depends on the uncertainty of the velocity estimations. As for the estimations of the convection velocity (u_c), it depends on the fitting procedure based on the work of [41]. A summary of the main PIV measurement and post-processing parameters is presented in Table 2.

Surface pressure microphones

The wall-pressure fluctuations on the serration are measured with an array of 10 surface-mounted sensors. Measurements are carried out for the the flap angles of $\delta_f = 0°$, 10°, and 15°. The O8AC03 MEMS sensors are installed on a printed circuit board (PCB) 0.2 mm thick (Fig. 2b,c), attached over the Plexiglas for non-intrusive instrumentation of the serration. Sensors are calibrated against a reference LinearX M51 microphone by measuring simultaneously an acoustic field band-passed within 50 Hz and 5 kHz (microphone linear range). The sensitivity of the microphones in average is of 18.4 mV/Pa with a variance in the estimations for each sensor in the order of 0.14 mV/Pa. This level of variance points to an uncertainty on the pressure estimations of ± 0.5 dB (95% reliability). It is important to highlight that this level of uncertainty is modified by other factors, such as temperature variations and the post-processing technique, e.g. the Welch's method. Table 3 summarizes the main characteristics and uncertainties on the analyses carried out with the sensors. Surface pressure data are recorded at a rate of 51.2 kHz during 30 seconds using a National Instruments cDAQ-9189 chassis and NI-9234 boards.

Phased array beamforming

Acoustic measurements are carried out with a 64-microphone array, visible in Fig. 1b also for the flap angles of $\delta_f = 0°$, 10°, and 15°. The array features a modified Underbrink spiral configuration, optimized to reduce beamwidth and minimize sidelobe levels for applications in the A-Tunnel [42]. The array uses G.R.A.S. 40PH microphones connected to a dedicated National Instruments PXIe system equipped with 4 PXIe-4499 boards. Data is acquired at 51.2 kHz for 30 seconds. The centre of the array is placed at 1 m distance from the model half-chord, resulting in an angle of 25° between the central microphone and the trailing edge.

Post-processing is carried out with the conventional beamforming technique (CBF) described by Sijtsma [43]. The time series is converted into a matrix of cross-spectral terms (CSM) to estimate source levels at desired locations within the model mean plane using the steering vector formulation I from the work of Sarradj [44]. Correction of the effect of the flow velocity on the acoustic wave propagation is carried out based on the average velocity between the source and the microphone [43]. The spurious noise produced by the tripping device is eliminated by removing the main diagonal of the CSM, containing the microphone auto-spectra. This process is important to reduce uncorrelated sources but also to avoid the contamination of the source maps by other acoustic sources [43]. Sound power levels at the trailing-edge region are estimated by the source power integration (SPI) procedure [45] in a 100×100 mm^2 area centred around the trailing-edge position ($X = 1h$).

Analytical models for turbulent boundary layer trailing-edge noise

A thorough investigation of the influence of the flow field on the scattered noise is based on the identification of the relevant flow quantities. Analytical models, such as that from Amiet [46], are important indicators of the main parameters affecting trailing-edge noise. According to the former work, the noise coming from the trailing-edge, located at $x_o = 0$, on an semi-infinite flat plate is described according to eq. (3). In the equation l_z is the spanwise correlation length, $u_c = \omega/k_x$ the convection velocity, $S_{pp}(\omega, x_o, y_o)$ the estimated acoustic spectrum at a location (x_o, y_o) along the airfoil mid-span ($z_o = 0$), c_o the speed of sound, b the model span, β the
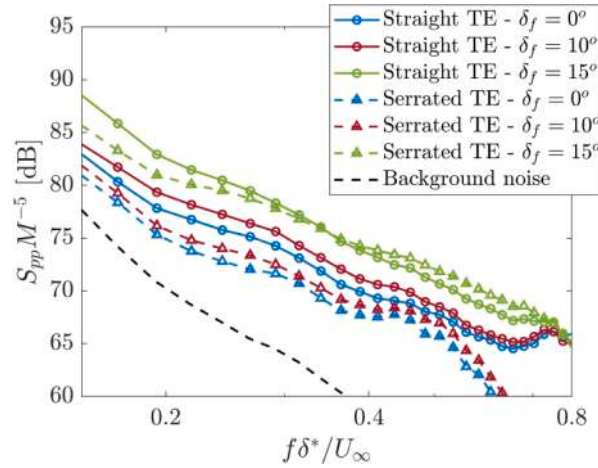
Fig. 3. Acoustic noise levels estimated from the SPI procedure of the CBF maps. Measurements are performed with a straight and a serrated trailing-edge insert at $\delta_f = 0°$, 10° and 15°.

Prandtl-Glauert factor, $\phi_{pp}(\omega)$ the wall-pressure spectrum, $R = \sqrt{x_o^2 + y_o^2}$ the trailing-edge distance to the observer, and $\mathscr{L}$ the scattering transfer function. The work of [47] have modified $\mathscr{L}$ in order to include the back-scattering effects at the model leading edge, therefore expanding the solution to a finite plate or airfoil. This latter formulation is used in this work to estimate the noise past the straight trailing edge.

$$S_{pp}(\omega, x_o, y_o) = \left[\frac{\omega R}{2\pi c_o \left(x_o^2 + \beta^2 y_o^2 \right)} \right]^2 |\mathscr{L}|^2 b \phi_{pp}(\omega) l_z(\omega) \tag{3}$$

The recent model from Ayton [9] provides a fully analytical solution for the acoustic scattering problem [48] on a serrated trailing edge of any shape. With the simplifications from Lyu and Ayton [14], the analytical solution is given by eq. (4), where E_n is now the scattering transfer function for a given serration geometry and acoustic wavenumber. The parameter $\Pi_{pp}(\omega, k_z)$ is the wall-pressure wavenumber-frequency spectrum and comprises the effects of $\phi_{pp}(\omega)$, and $l_z(\omega)$ at the serrated trailing edge. Similar to Amiet's model, Taylor's frozen turbulence assumption [11] is also required to apply this formulation.

$$S_{pp}(\omega, x_o, y_o) = \frac{K}{2\pi^2 R} \frac{\beta^2 k_x + K}{\left[\beta^2 k_x + K\cos(\theta) \right]^2} \sin(\theta/2) \sum_{m=-\infty}^{+\infty} \Pi_{pp}(\omega, k_z = 2\pi m/\lambda) |E_n(-K\cos\theta/\beta)|^2 \tag{4}$$

The wavenumber frequency spectrum can be obtained following the generalization proposed by Roger and Moreau [47] based on the work of Corcos [49] (eq. (5)), which predicts maximum energy for $k_z = 0$ and $\Pi_{pp} \propto \phi_{pp} l_z$, similarly to the contribution of the aerodynamic fluctuations in eq. (3). This quantity is used in Section 4.2 to represent the input from the wall-pressure fluctuations along the serration edge to the scattered noise.

$$\Pi_{pp}(\omega, k_x = \omega/u_c, k_z) = \frac{1}{\pi} \phi_{pp}(\omega) \frac{l_z(\omega)}{1 + [k_z l_z(\omega)]^2} \tag{5}$$

The streamwise and spanwise correlation lengths (l_x and l_z respectively) are computed as the integral of the coherence function of the surface pressure fluctuations between two wall locations, following the definition provided by Amiet [46]. According to Lyu et al. [10], the streamwise correlation length (l_x), despite not explicitly present in the equation above, is another parameter that affects the noise reduction performance of serrated trailing edges. An exponential curve-fit following the model of Corcos [50] is used here to compute the integral, reducing the influence of measurement noise at low correlation levels. The convection velocity (u_c) is estimated with the phase shift between two measurement points separated in the streamwise direction, according to the work from Romano [41]. Following Corcos [50], the latter parameter can be connected to the correlation length with eq. (6), where α_x and α_z are, respectively, the constants for the streamwise and spanwise correlation lengths.

$$l_{x,z}(\omega, k_z) = \frac{u_c}{\alpha_{x,z} \, \omega} \tag{6}$$

In the present work, a connection between the pressure and the velocity field is attempted considering the flow field distortions featured by the serrated trailing edge under aerodynamic loading. To this purpose, the terms of the Poisson equation for pressure (Panton and Linebarger [40], Eq. (7)) are studied using the velocity inputs from the PIV data. In the equation $\overline{u}_i$ and u_i represents the mean and fluctuating velocity components respectively, $\overline{u_i u_j}$ the Reynolds stress tensor components, and ρ the flow density. In the modelling from Panton and Linebarger, the two terms on the right-hand side are named mean shear and turbulence interaction (MS-T)
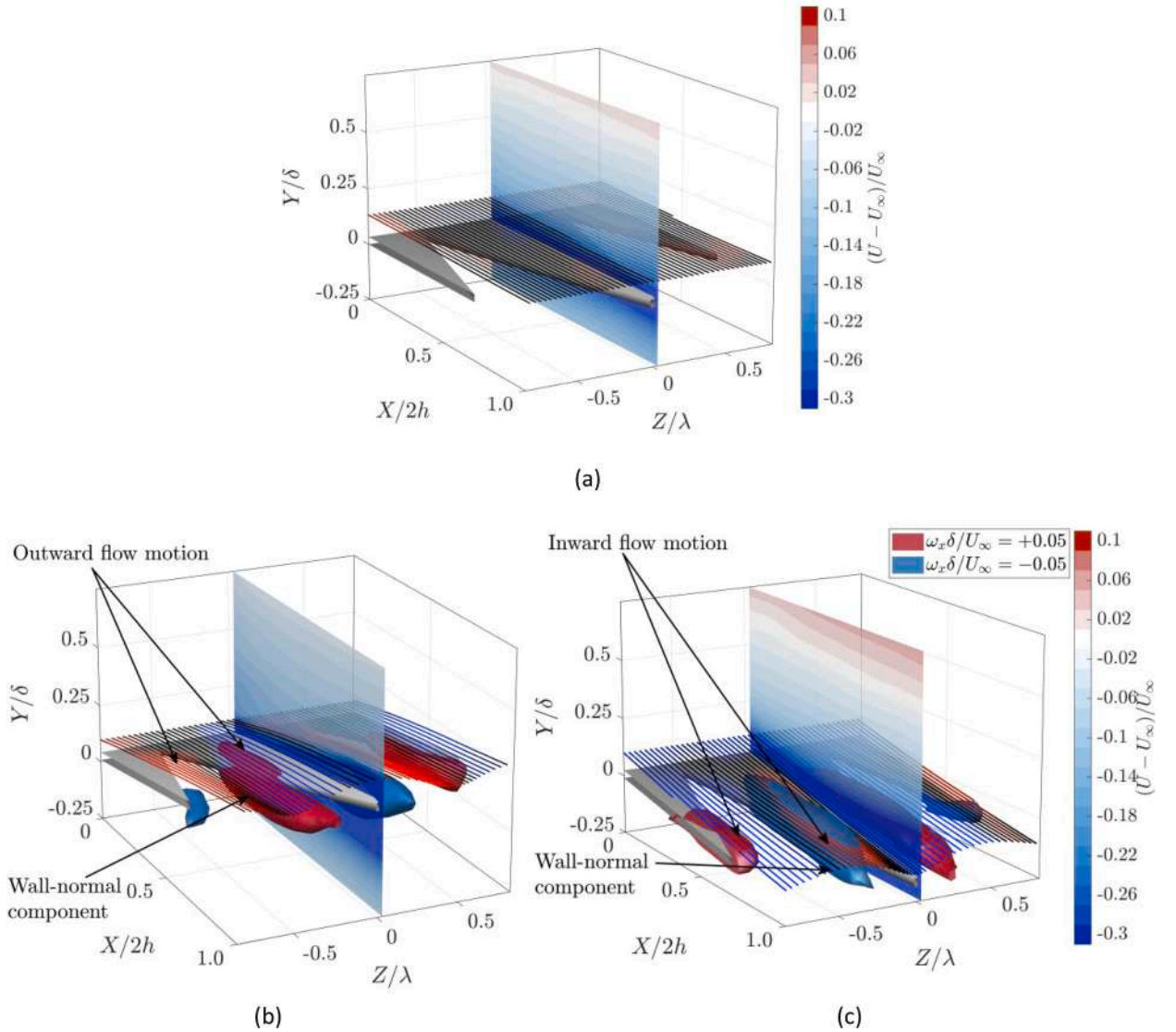
Fig. 4. 3D visualization of the mean flow over the trailing-edge serration at $\delta_f = 0°$ (a) and $\delta_f = 10°$ from the pressure (b) and suction side (c). Isosurfaces of streamwise vorticity are shown in red ($\omega_x \delta^*/U_\infty = +0.05$) and blue ($\omega_x \delta^*/U_\infty = -0.05$). Streamlines of the flow at $Y/\delta = 0.1$. Black streamlines are undistorted, red and blue correspond to $w \geq 0.04U_\infty$ and $w \leq -0.04U_\infty$ respectively.

and the turbulence self-interaction (TT) respectively. The latter term can usually be neglected [12,51] as demonstrated by Jaiswal et al. [52] for the flow inside a turbulent boundary layer. The MS-T term represents the pressure fluctuations that are caused by the interaction between the velocity fluctuations and the mean flow gradients. This can be further simplified, as presented by Panton and Linebarger [40], for a turbulent boundary-layer flow, where the streamwise velocity derivatives along the wall-normal direction dominate ($\frac{\partial \overline{u}}{\partial y} \frac{\partial v}{\partial x}$).

$$\frac{\partial^2 p}{\partial x_i^2} = -2\rho \frac{\partial \overline{u}_i}{\partial x_j} \frac{\partial u_j}{\partial x_i} - \rho \frac{\partial^2}{\partial x_i \partial x_j} \left(u_i u_j - \overline{u_i u_j} \right) \qquad (7)$$

Results

Flow and noise properties from trailing-edge serrations

The overall contribution of the serration on the far-field noise measurements is presented and compared to the straight configuration (Fig. 3). As can be seen from the results, the serrated trailing-edge geometry is responsible for reducing the far-field noise compared to the straight trailing edge at almost all the tested conditions. Noise reduction over the entire frequency range is observed
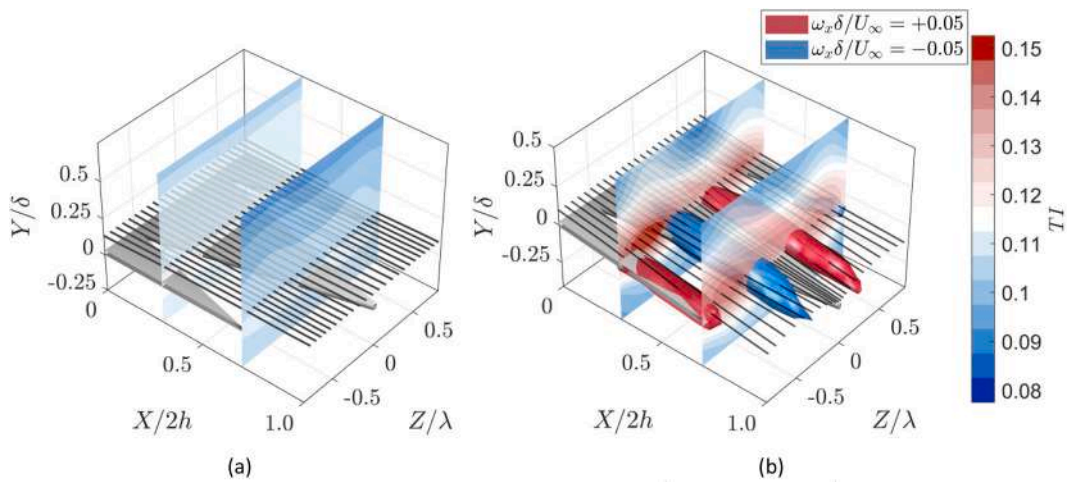
Fig. 5. Spatial distribution of turbulence intensity (TI) at $\delta_f = 0°$ (a) and $\delta_f = 10°$ (b) by cross-sections at $X/2h = 0.25$ and 0.75. Isosurfaces of streamwise vorticity as from fig. 4. Black lines show the streamlines of the flow at 8 mm from the wall.
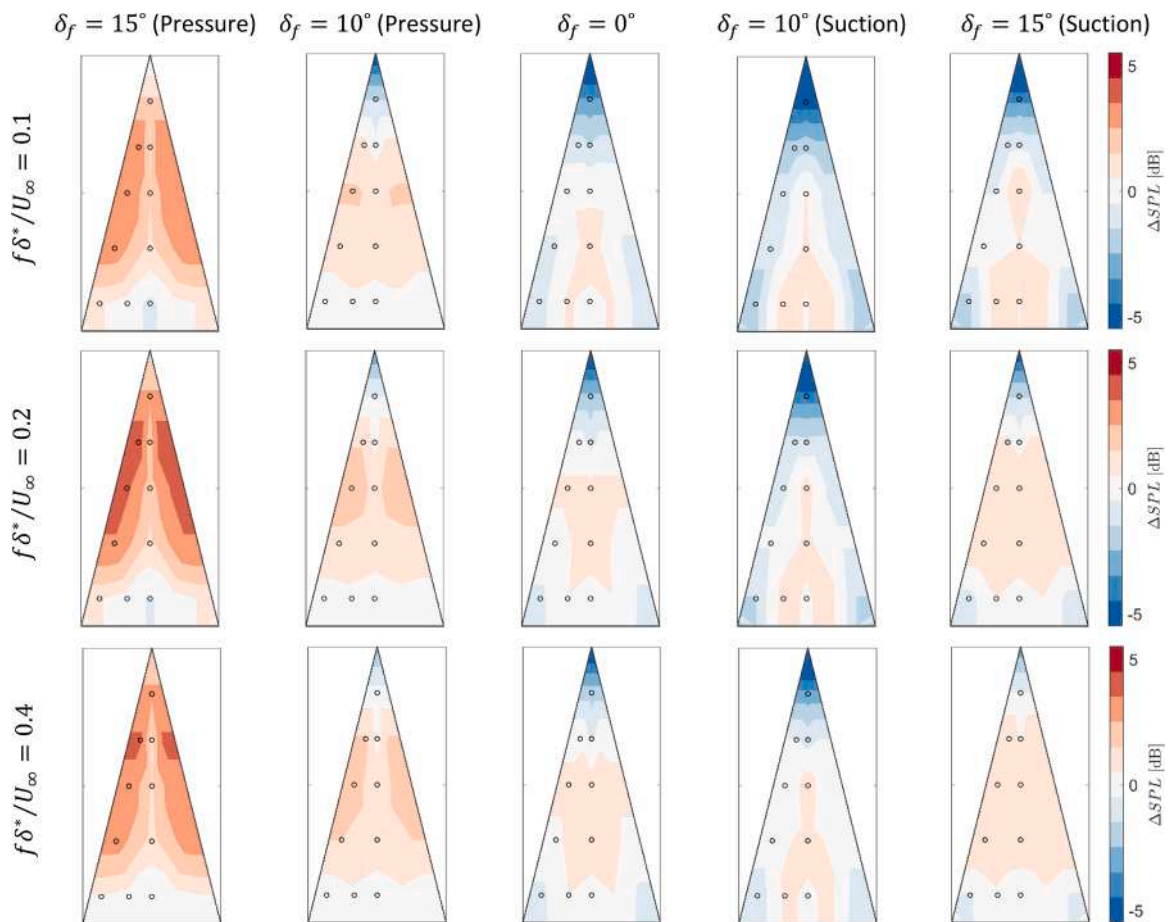

Fig. 6. Surface pressure fluctuations along the trailing-edge serration relative to the incoming level (reference Mic 09). Trailing-edge incidence angle δ_f varies along columns. Strouhal number varies across rows. The circles represent the position of the sensors. Data is measured on half serration and mirrored for visualisation purposes.

for both the $\delta_f = 0°$, and the $\delta_f = 10°$ cases. However, for the largest value of the flap angle ($\delta_f = 15°$) the noise from the serrated trailing edge increases when $f\delta^*/U_\infty > 0.3$. This result is consistent to previous works from Arce León et al [7], and Gruber et al. [8] who ascribe it to the alterations of the flow caused by the serrations under loading.

An indication of the physical cause of the noise alterations is given by the time-averaged flow field over the trailing-edge serrations at $\delta_f = 0°$, and $\delta_f = 10°$, plotted in Fig. 4. Planar contours of the time-averaged velocity magnitude in the centre of the serration are plotted together with iso-surfaces of positive and negative streamwise vorticity.

Three main flow regions can be identified, i.e. the incoming turbulent boundary layer over the serration surface, the developing wake along the gaps in-between the serrations, and the trailing vortices at the serration edges. At $\delta_f = 0°$, streamlines deflection is barely observed. When the serrations are loaded ($\delta_f = 10°$), the pressure mismatch between the suction and pressure side induces a pair of streamwise vortices along the serration edges. These vortices are visible in the figure from approximately 25% of the serration height. Similar to what was shown by Avallone et al. [53], the vortices are formed along the edges in the centre of the serration and are approximately aligned with the free-stream direction.

A visible deflection of the streamlines with respect to the $\delta_f = 0°$ case is therefore introduced, indicating that the flow presents accelerations. As a consequence, velocity gradients are generated along the spanwise and wall-normal directions. Contrary to the wall-normal deflection, the spanwise one is relatively small to be seen from the pictures. To improve the visualization of this component, the regions where the streamlines have a spanwise velocity above $w = +0.04U_\infty$ are represented in red, while the regions where this velocity component is smaller than $w = -0.04U_\infty$ are represented in blue. For $\delta_f = 10°$, on the pressure side, the streamlines deflect towards the gap of the serration because of the higher pressure along the serration centre line; on the suction side, the exact opposite happens with a deflection towards the centre line of the serration region, highlighted by the inversion of the streamline colour pattern. The alterations of the streamlines demonstrate the presence of spanwise velocity gradients, which are accentuated along the edges of the serration. At this region, the flow direction is modified, with respect to the incoming flow direction, by about 4° along the spanwise direction and by about 6° along the wall-normal direction in the gap region. These deflections were observed by Arce León [7], who concluded that the noise increase cannot be explained by simply considering the altered flow direction on the scattering function of Howe [6]. From the work of Arce León [7], the increase in noise observed at high loading conditions was conjectured to have a direct relation with the flow distortions induced by the trailing vortices on the fluctuations near the edges of the serrations.

The spatial distribution of the turbulent intensity (TI) over the serration can be visualized in Fig. 5 for $\delta_f = 0°$, and $\delta_f = 10°$. The plot shows two streamwise aligned planes, one at 25% and another at 75% of the serration height. At $\delta_f = 0°$ the turbulence intensity near the wall attains about 8%U_∞. From root to tip only a small dissipation occurs and no significant variation along the spanwise direction is captured. At $\delta_f = 10°$ a region of high turbulence intensity emerges at the gap in between the serration. The intensity of the turbulent fluctuation at this region is stronger at the root and dissipates towards the serration tip, as observed in the numerical studies of Jones and Sandberg [20]. Turbulence intensity is as high as 15%U_∞, about 2%U_∞ higher than the one captured around the centre of the serration. Previous works [7,20] concluded that the interaction between this region of increased turbulent flow and the accelerating vortex pairs field, ultimately affects the distribution of the wall-pressure fluctuations over the serration, causing the increase in noise observed for trailing-edge serrations under loading.

Wall-pressure fluctuations over serrations

The spatial distribution of the surface pressure fluctuations obtained from the installed microphones is illustrated in Fig. 6. Columns correspond to varying incidence of the trailing-edge insert from $\delta_f = 0°$ to $\delta_f = 15°$ (both on the pressure and suction side). The analysis is presented for three selected frequency bandwidths. The chosen values of the frequency expressed in non-dimensional form are $f\delta^*/U_\infty = 0.1, 0.2$, and 0.4 respectively. Data are reported in terms of the difference of Sound Pressure Level (ΔSPL) between the signal at each microphone and M09, i.e. the microphone located at the root of the serration ($X/2h = 0.1, Y/2h = 0$), taken as a reference for the incoming wall pressure from the turbulent boundary layer. The graphs represent an illustration of the spatial distribution of the wall-pressure fluctuations on the serration surface. For visualisation purposes, the data points are spatially (linearly) interpolated such to yield the visualization with colour-contours. Linear extrapolation is applied towards the outer edges. Moreover, symmetry is assumed to complete the spatial distribution over the serration surface. The visualization clearly indicates a spatial variation of the surface pressure fluctuations along the streamwise as well as the spanwise direction. The latter indicates that assuming frozen turbulence is inadequate to accurately model the overall noise reductions from loaded serrations. It is hereby assumed that the modifications captured from the wall-pressure sensors are mostly caused by the modification of the aerodynamic flow conditions. Given the low Mach number and the large separation between aerodynamic and acoustic wavenumbers, the acoustic field over the serrations is expected to remain uniform within the serration length.

At $\delta_f = 0°$, only mild variations of pressure fluctuations are observed on the main body of the serration (up to the half-height). Towards the tip of the serration, a marked reduction of the pressure fluctuations is observed. Similar behaviour was reported by Avallone et al. [54] for the pressure RMS fluctuations. This behaviour is observed at almost all conditions and is ascribed to the diminished wall effect when flow structures are only partly bounded by the solid wall.

The trend is accentuated when considering the suction side for the $\delta_f = 10°$ case and for Strouhal numbers $f\delta^*/U_\infty < 0.2$. At this condition, the higher incoming pressure fluctuations, compared to the $\delta_f = 0°$ case, rapidly decrease from the root of the serration towards the serration edges because of the decreasing pressure gradients along the serration gap. On the pressure side, a noticeable increase of the pressure fluctuations with respect to the incoming one is captured at the edges of the central portion of the serration. This increase corresponds to the location of the vortex pair and mostly impacts the pressure fluctuations at 25-75% of the serration
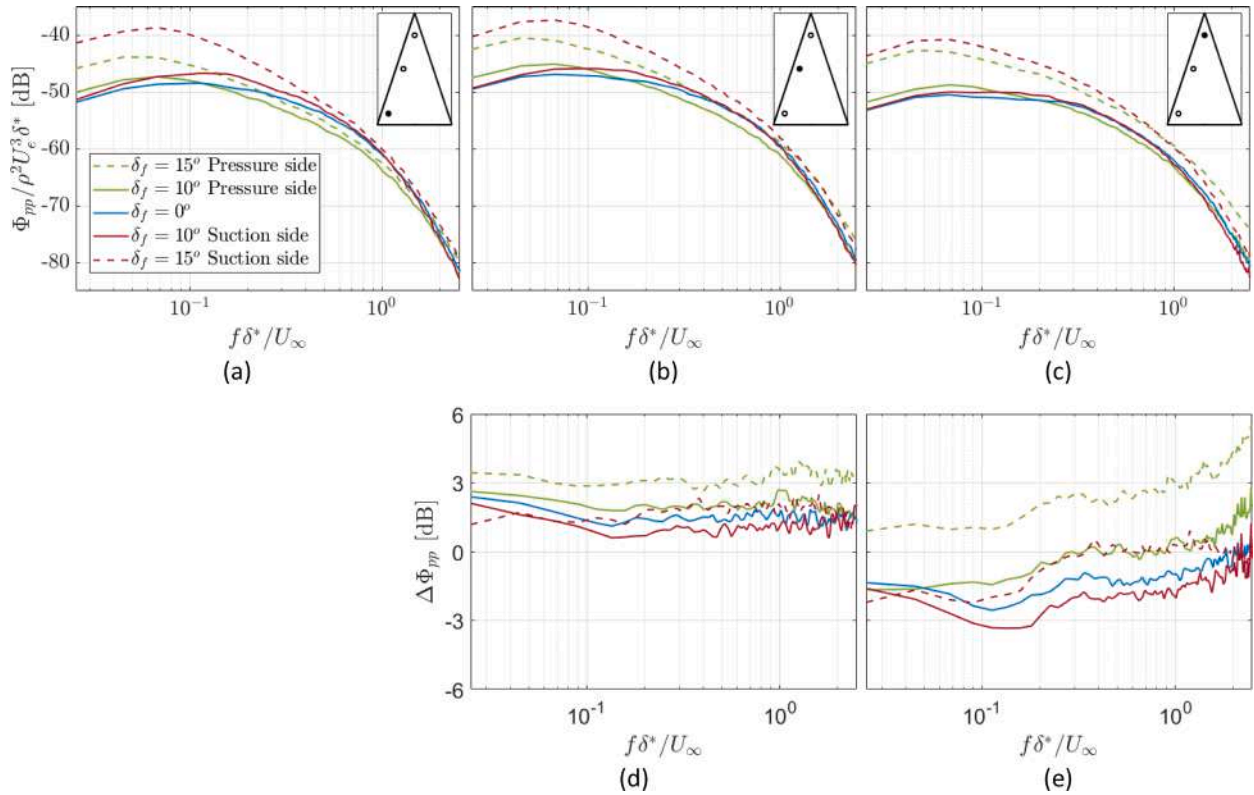
Fig. 7. Variation of the wall-pressure spectrum along the serration edge and relative change in relation to $X/2h = 0.1$ at $X/2h = 0.1$ (a), $X/2h = 0.5$ (b and d), and $X/2h = 0.8$ (c and e).

height. In the condition of highest loading ($\delta_f = 15°$), this effect is most pronounced with significantly higher wall-pressure fluctuations along the edges of the pressure side and a minor increase also noted on the suction side.

The above discussion stresses the role played by the different flow regimes around the serration whereby three types of flow may be identified, namely the incoming turbulent boundary layer, the near wake region in-between the serrations, and the vortex pairs along the serration edges. When the aerodynamic loading is small, the pressure over the serration is ascribed only to the turbulent boundary-layer flow and the influence of the gap region. This yields a reduction in the pressure spectrum along the edges and tip of the serrations, as captured for the $\delta_f = 0°$ case and on the suction side for the $\delta_f = 10°$ test case.

At higher loading conditions, the increasing pressure fluctuations induced by the trailing vortices dominate over those transported within the turbulent boundary layer, and new regions with higher pressure fluctuations emerge along the edges of the serration. These regions appear to be concentrated at the central portion of the serration at lower frequencies, while they become stronger and extend towards the tip at higher frequencies, e.g. $f\delta^*/U_\infty = 0.4$. The influence of the vortex pairs is clear for the $\delta_f = 10°$ case on the pressure side and for the $\delta_f = 15°$ on both sides. The combination of these two patterns, viz. reducing wall pressure towards the tip and increasing levels along the edges, determines the distribution of wall-pressure fluctuations observed in the present experiments. The velocity gradients induced by the vortex pairs forming on the pressure side combined with the lower incoming pressure fluctuations from the FPG boundary layer, leads to a stronger spatial alteration of the wall-pressure fluctuations at this side, as discussed in Jones and Sandberg [20], and Arce León et al. [7]. On the other hand, the suction side perceives the influence of the shear along the edges only at extreme loading conditions ($\delta_f = 15°$).

The effect of the aerodynamic mechanisms presented above on the spectral distribution of the wall pressure can be observed in Fig. 7 where the wall-pressure spectra are presented for different values of the flap angle. Fig. 7 (a, b, and c) show the pressure spectra at $X/2h = 0.1$ (root), $X/2h = 0.5$ (centre) and $X/2h = 0.8$ (tip) normalised by the freestream velocity and boundary-layer displacement thickness at the ZPG condition. The sensors closer to the edge are selected as the scattering is more strictly related to the wall-pressure fluctuations at the edge. Fig. 7d and 7e show the variation of the pressure spectrum ($\Delta\phi_{pp}$) with respect to the root region (sensor M05).

Here an increase of the wall-pressure spectrum at the serration centre followed by a decrease at the tip for the $\delta_f = 0°$ case become apparent. However, at the tip, an increase in the levels is noted in the high-frequency range. This was also observed in previous studies with numerical simulations [19] where it was hypothesized to be due to the development of additional small structures generated in the wake around the serration tip.

At $\delta_f = 10°$, the APG boundary layer on the suction side exhibits an overall increase of the pressure fluctuations while the FPG one on the pressure side exhibits a low-frequency increase followed by a decrease for $f\delta^*/U_\infty > 0.1$. This observation is expected for
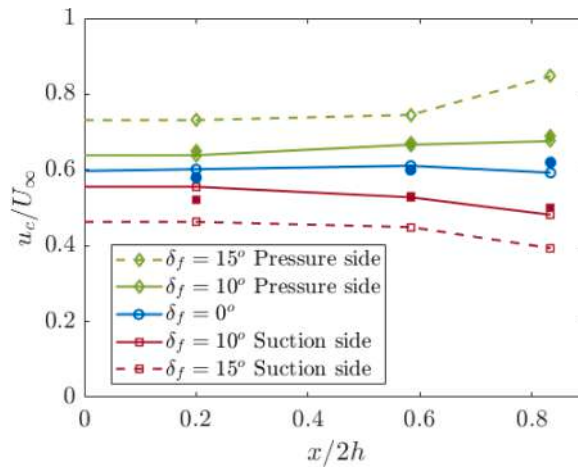
Fig. 8. Wall-pressure convection velocity estimated along the centre of the serration. Filled marks represent estimations from PIV measurements.
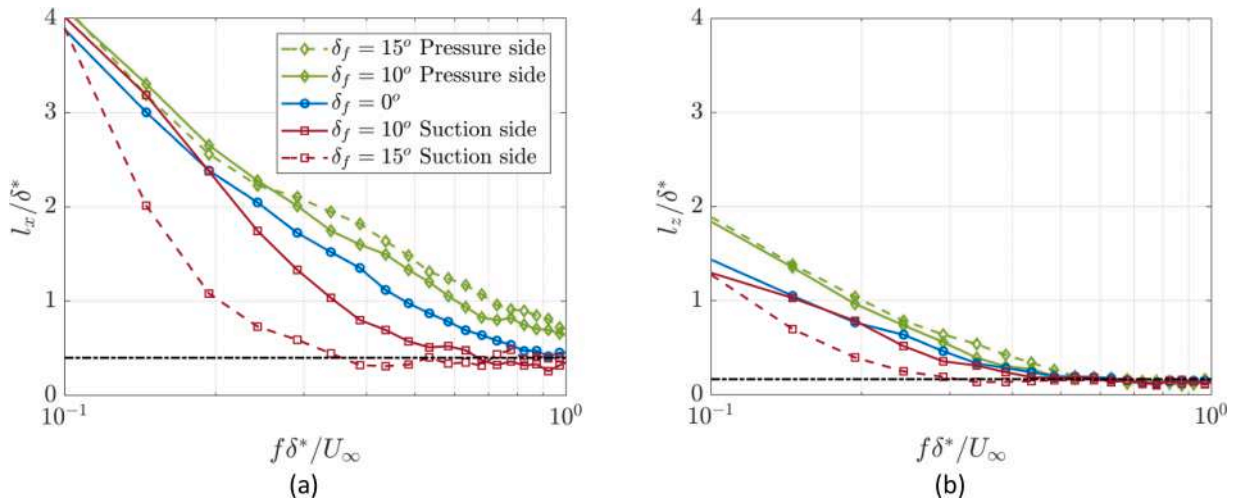

Fig. 9. Measured streamwise and spanwise correlation length along the trailing-edge serration from the surface microphone sensors at $\delta_f = 0°$, $10°$, and $15°$. The black dot-dashed lines represent the limit of the measurement technique considering coherence levels below 0.05 for two adjacent microphone sensors.

conditions of mild pressure gradient turbulent boundary layers, as demonstrated by Hu and Herr [55]. As the flow advances along the edges of the serration, the amplitude of the pressure fluctuations on both sides slowly converge to the ZPG condition, as can be seen in Fig. 7b, and c. This indicates that the high overall levels on the suction side decrease more rapidly compared to the ones on the pressure side ($f\delta^*/U_\infty > 0.1$).

Results at $\delta_f = 15°$ differ from the $\delta_f = 0°$, and $10°$ case. The overall levels at the root are increased on both sides, with the suction side dominating the amplitude of the pressure fluctuations. Along the edges, the vortex pairs seem to induce a significant increase in the wall-pressure levels, which can be observed by comparing the variation in Fig. 7d and e with respect to the $\delta_f = 10°$. This overall increase of the wall-pressure fluctuations along the edges of the serration affects the levels measured at the centre and tip of the serration, where the suction and pressure sides reach similar levels, with the pressure side dominating the pressure fluctuations in the frequency range above $f\delta^*/U_\infty = 1.0$.

The previous observations can be used to attempt a first description of the overall effect of aerodynamic loading on the distribution of the wall-pressure fluctuations over the serration surface. The footprint of the pressure fluctuations at zero or mild loading displays a maximum at the root and centre of the serration and a decrease along the serration edges. At these conditions, the influence of the open region beneath the serrations progressively reduces the pressure fluctuations, consequently reducing the pressure fluctuations at the edge. As the loading increases, the onset of the vortex pair increases the shear along the edges of the serration and consequently the pressure-fluctuation levels around this region.

As mentioned in Section 3, besides the wall-pressure spectrum levels, the study of the spatial distribution and convective properties of the wall-pressure fluctuations along the serration is necessary to fully represent the parameters playing a role in the modelling of the
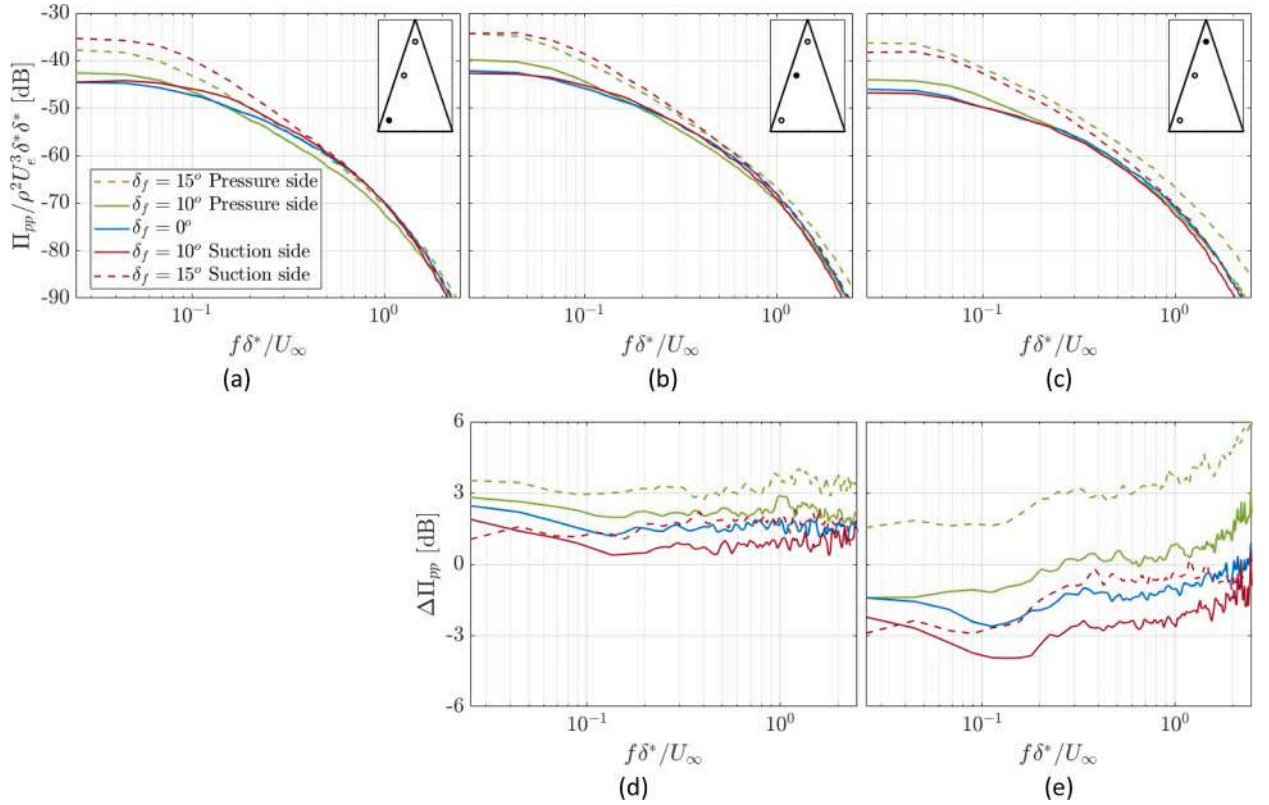
Fig. 10. Variation of the scattering energy spectrum along the serration edge and relative change in relation to the root (X /$2h = 0.1$), at X /$2h =$ 0.1 (a), $X/2h = 0.5$ (b and d), and $X/2h = 0.8$ (c and e).

scattered noise. The convection velocity estimated from the sensors (lines) along the centreline of the serration is presented in Fig. 8. Estimations from PIV measurements along the serration edges are presented too (filled marks). The agreement between the microphone- and the PIV-based estimations indicates that the convection velocity does not change significantly along the spanwise direction. At zero pressure gradient, the advection of the pressure fluctuations is sustained at 59% of the free stream velocity. Following the boundary-layer velocity profile on the pressure side, a higher velocity closer to the wall is due to the effect of the locally favourable pressure gradient. This is responsible for increasing the velocity with which the turbulent eddies that cause the wall-pressure fluctuations are transported, consequently increasing the convection velocity. Conversely, on the suction side, the fluctuations near the wall are transported at a lower mean velocity. Therefore a lower convection velocity is expected for the wall-pressure fluctuations, as observed from the measurements. From the root to the tip, u_c increases on the pressure side and decreases on the suction side. Avallone et al. [53] have also observed an increase in the convection velocity under similar conditions.

Compared to the baseline value of $u_c/U_\infty = 0.6$, the maximum flap angle causes a decrease of the convection velocity to 0.4 on the suction side and an increase to 0.8 on the pressure side. These modifications impact the correlation length of the flow structures on the serrations at a given frequency. Following the formulation of Corcos [49], the stream and spanwise correlation lengths are proportional to the convection speed. Therefore, the higher u_c is, the higher the correlation length of structures at a given frequency and, consequently the energy scattered at the trailing edge.

Fig. 9 presents the correlation lengths in span and streamwise direction (calculated from the wall-mounted sensors) at the root of the serration. Overall, results seem to agree with Corcos [49] formulation (see Appendix A for direct comparisons), and larger correlation lengths are captured on the pressure side and lower ones on the suction side for the same Strouhal numbers. A fitting process with the obtained curves using Corcos [49] formulation yields a constant $\alpha_x \approx 0.17$ for the streamwise correlation length and $\alpha_z \approx 0.70$ for the spanwise correlation length, similar to the values described by Hu and Herr [55], ($\alpha_x = 0.15$, and $\alpha_z = 0.72$).

The increased length of the coherent structures on the pressure side indicates that, although the captured levels at this side are overall lower, the structures are correlated throughout a larger extension. This implies that the coherent scattering from such structures at the trailing edge is stronger and should be considered together with the wall-pressure levels.

A final assessment of the contribution from the correlation length and pressure levels to the trailing-edge noise can be carried out with the highest wavenumber-frequency wall-pressure spectrum mode ($\Pi_{pp}(\omega, k_y = 0) \propto \phi_{pp}(\omega) l_z(\omega)$) along the serration (Fig. 10). The plot combines the variations of the wall-pressure spectrum (Fig. 7) with the ones of the spanwise correlation length (Fig. 9) at different regions of the serration. Fig. 10a, b, and c show the wall pressure at the root, centre, and tip of the serrations respectively. Fig. 10d, and e show the difference in levels ($\Delta\Pi_{pp}$) with respect to the condition at the root (sensor M05).
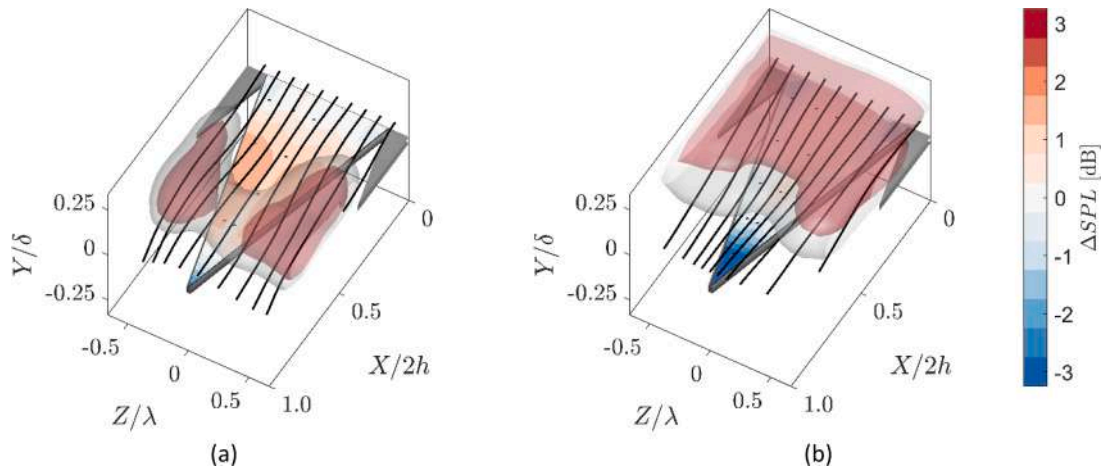
Fig. 11. Iso-surfaces of the MS-T term (bandpass filtered at $f\delta^*/U_\infty = 0.4$) compared against the surface pressure measurements from the microphones on the pressure (a) and suction side (b) of the flat plate at $\delta_f = 10°$. The iso-surfaces represent non-dimensional levels MS-T of 0.025 (grey surface) and 0.04 (red surface). Pressure fluctuations are taken from Fig. 6.

At $\delta_f = 0°$, the value of Π_{pp} reaches a maximum in the centre (higher pressure and convection velocities) and decreases at the tip, indicating that noise, in this condition, is primarily dominated by the scattering of acoustic waves at the edges of the serrations located at the root and central portion of the serration. Nevertheless, the small differences captured along the serration surface suggest that the contribution from the other portions of the serration is not negligible.

The wall-pressure fluctuations from the pressure side are significantly impacted by the effect of the vortex pairs. The increasing levels in the centre and tip of the serration and the extended length of the turbulent structures are responsible for bringing the wall-pressure levels on the pressure side closer or even higher than the conditions on the suction side. In the centre of the serration, the pressure side dominates the scattering at very low ($f\delta^*/U_\infty < 0.1$, $\delta_f = 10°$) and very high frequencies ($f\delta^*/U_\infty > 1.0$, both flap angles). At the tip, Π_{pp} is higher on the pressure side for both flap angles tested.

It can be confirmed from the study that, at low and mid-frequencies ($f\delta^*/U_\infty < 0.2$), the scattering on the serration is dominated by the conditions at the serration root and centre whereas the tip becomes important only at high frequency, as also suggested in the numerical work of Avallone et al. [19]. Moreover, the suction side is seen to dominate the wall-pressure fluctuations at the root and centre while the pressure side increases its importance in the centre while dominating the noise generation at the serration tip, as previously indicated by Arce León et al. [17].

Vortex pairs and wall-pressure fluctuations

The previous results have been used to characterize the flow near the trailing-edge serration and the spatial and temporal distribution of the wall-pressure fluctuations. A qualitative comparison is presented here, whereby the three-dimensional flow field and the surface pressure distribution are examined with the aim to identify the effect of streamwise vortices on the wall-pressure distribution. Here, the Poisson equation for pressure is invoked (eq. (7)), which relates the pressure fluctuations with regions of accelerating turbulent flow at its surroundings. This section analyses the variations in the MS-T source term. It is hereby assumed that the variations of the MS-T term are solely related to the variations on the intensity of the pressure fluctuations. This analysis seeks for indications of the causes for the modifications of the wall-pressure observed in the previous section. It is important to highlight that the MS-T is related to the wall-pressure by a volume integration, according to [51], and this analysis provide only an indication of the regions where the MS-T variation are more intense.

Iso-surfaces of the MS-T source term (eq. (7)) can be visualized in Fig. 11 together with the associated pressure fluctuations at the wall measured from the surface-mounted microphones (taken from Fig. 6) for $\delta_f = 10°$. The data are bandpass at $f\delta^*/U_\infty = 0.4$. The regions with higher pressure fluctuations can be correlated to those of high MS-T fluctuations on the flow. This supports the conjectures of Section 4.1 between the formation of secondary flow structures and their relation to the pressure fluctuations. In particular, the MS-T fluctuations attain a maximum at approximately one momentum thickness above the surface, where the mean-flow gradients of the turbulent boundary layer interact with the stronger velocity fluctuations.

The pressure side exhibits overall low MS-T levels with respect to the $\delta_f = 0°$ case and pressure fluctuations are only increased along the edges of the serration, where the vortex pairs are active, following the regions where the streamlines are more strongly deflected.

On the suction side, high values of MS-T are observed at the root and central portion of the serration, following the high incoming turbulence levels from the adverse pressure gradients observed in Fig. 5b. This behaviour was also reported by Avallone et al. [53] for the suction side of a sawtooth serration at 4° angle of attack. A secondary region of increased MS-T is captured along the gaps of the serration and is linked to the spanwise accelerations imposed by the vortex pairs along the edge, also in agreement with the region of high-pressure fluctuations.
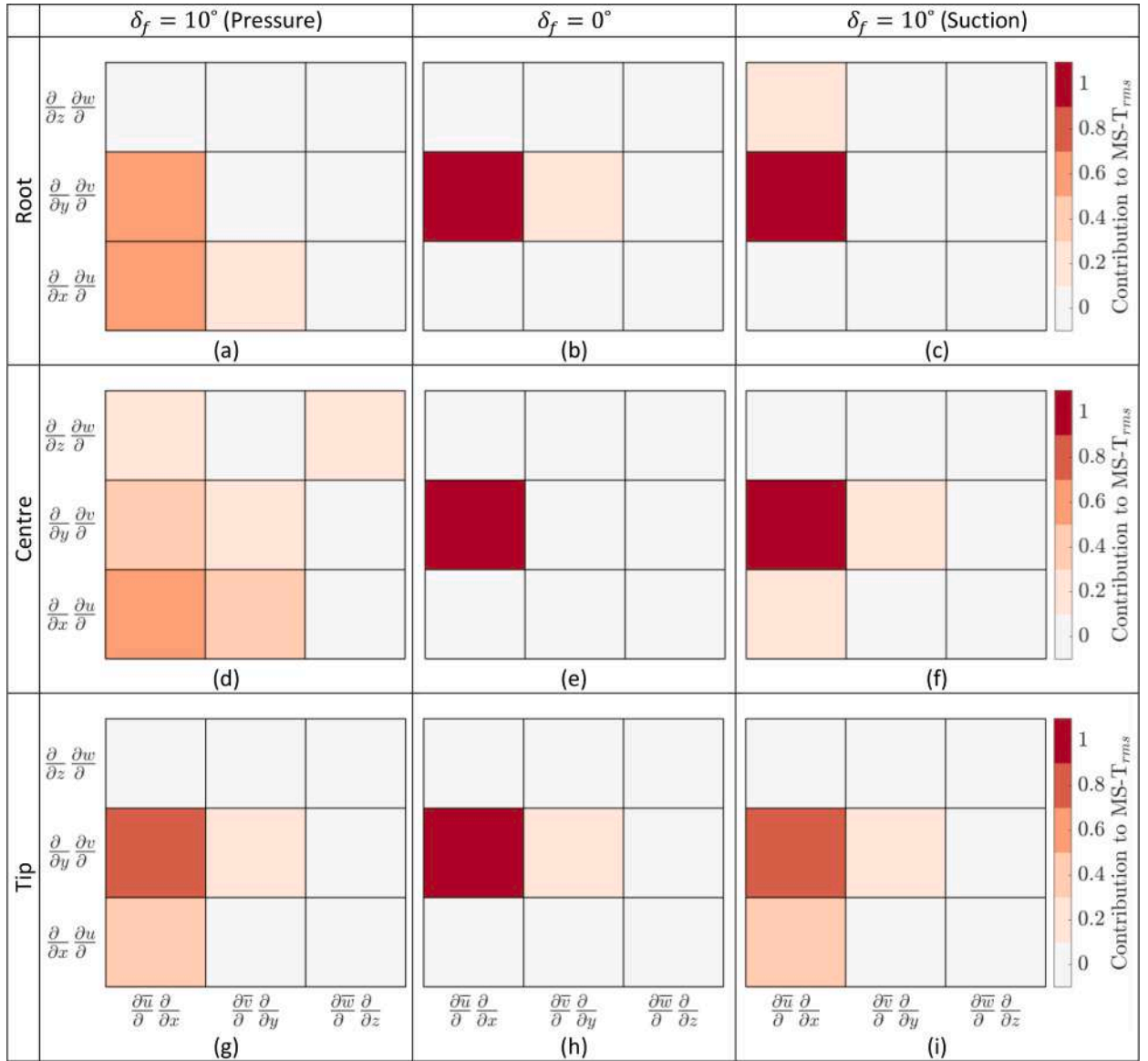
Fig. 12. Relative contribution of the root-mean-squared of each component $\frac{\partial \overline{u}_i}{\partial x_j} \frac{\partial u_j}{\partial x_i}$ to the mean shear-turbulence (MS-T) interaction term of the pressure Poisson equation estimated along the edges of the serration (one momentum thickness above the wall). Different flap angles, $\delta_f = 0°$ (b, e, and h) and $\delta_f = 10°$ on the pressure (a, d, and g) and suction sides (c, f, and i) are represented.

The previous results indicate that the distribution of the wall-pressure fluctuations over the serration surface is a direct consequence of the velocity gradient imposed by the mean flow on the incoming turbulent fluctuations (MS-T term) near the wall. Theoretical predictions of the wall-pressure fluctuations on a turbulent boundary layer are based on the dominant wall-normal shear (MS $-$ T $\sim -2\rho \frac{\partial \overline{u}}{\partial y} \cdot \frac{\partial v}{\partial x}$). Nevertheless, the MS-T term ($-2\rho \frac{\partial \overline{u}_i}{\partial x_j} \cdot \frac{\partial u_j}{\partial x_i}$) still comprises the sum of 9 different terms. Thus, a breakdown of each component of the MS-T interaction term can be used to indicate the contribution of the secondary velocity components to the wall-pressure fluctuations along the serration seen in Fig. 11, and the validity of the previous assumption for the flow over the serration.

Fig. 12 shows each of the 9 terms with respect to the total root mean squared value obtained at three different points of the edge of the serration (root, centre, and tip of the serration) for $\delta_f = 10°$. The values are obtained at one momentum thickness above the wall, following the region of more intense MS-T fluctuations observed in Fig. 11. In the figures, the terms are varied in i along the horizontal axis and in j along the vertical one. The overall sum does not equal 1 since this procedure neglects the coherent contribution of the components. Nevertheless, a maximum deviation of 30% of the total MS-T root mean square term is observed, indicating that the uncorrelated sum still holds most of the energy content in the domain.

The $\delta_f = 0°$ case shows the dominance of the $\frac{\partial \overline{u}}{\partial y} \cdot \frac{\partial v}{\partial x}$ term all over the serration, in agreement with the studies of Lilley and Hodgson
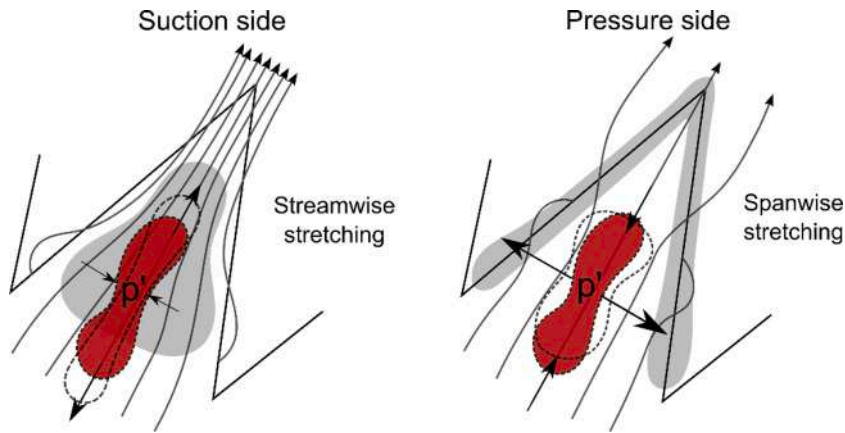
Fig. 13. Illustration of the flow mechanism acting on the suction (left) and pressure (right) side of an aerodynamically loaded serrated trailing edge. The red curve surface and arrows represent the eddy stretching mechanism, responsible for the associated increase in pressure fluctuations. The grey shades represent the regions where higher pressure fluctuations were captured in the measurements.

[51]. The latter term also dominates the Poisson source term on the suction side of the $\delta_f = 10°$ case, although a significant contribution of the $\frac{\partial \bar{u}}{\partial x} \cdot \frac{\partial u}{\partial x}$ and $\frac{\partial \bar{v}}{\partial y} \cdot \frac{\partial v}{\partial y}$ terms is captured at the tip (totalizing 45% of the total term root-mean-square). The finding is associated with the acceleration of the flow in the stream and wall-normal directions along the central portion of the serration (induced by the adverse pressure gradient) and the consequent changes in the corresponding velocity fluctuations captured. The results suggest that a description of the boundary layer and wake flow near the serration root suffices for the modelling of the wall-pressure fluctuations on the suction side under mild loading conditions. Besides, the predominance of the $\frac{\partial \bar{u}}{\partial y} \cdot \frac{\partial v}{\partial x}$ term indicates that current models of the wall-pressure spectrum can still be used.

This scenario is different for the pressure side. The reduced fluctuations from the favourable pressure gradient conditions hinder the influence of the wall-normal component ($\frac{\partial \bar{u}}{\partial y} \cdot \frac{\partial v}{\partial x}$) while the significant span and wall-normal accelerations of the mean-flow field along the serration lead to an increasing contribution from the secondary terms.

At the root and tip, the gradients of the velocity components in the streamwise direction also increase the importance of the $\frac{\partial \bar{u}}{\partial x} \cdot \frac{\partial u}{\partial x}$ term. However, the central portion of the serration is also influenced by the spanwise derivative components. Particularly, the increasing spanwise velocity along the edge due to the presence of the vortex pairs causes the terms $\frac{\partial \bar{u}}{\partial z} \cdot \frac{\partial w}{\partial x}$, and $\frac{\partial \bar{w}}{\partial z} \cdot \frac{\partial w}{\partial z}$ to contribute to 30% of the total MS-T fluctuation. These observations, coupled with the increased MS-T term along the serration edges, suggest that the increase in pressure fluctuations captured on the pressure side occurs due to the compression of the turbulence eddies in the streamwise direction. This process is strengthened at the sides of the serration due to the stretching of these eddies in the spanwise and wall-normal directions prescribed by the vortex pairs.

In summary, the conclusions that can be drawn from the above discussion are:

1) Pressure fluctuations are significantly modified throughout the serration and, as the loading over the serration is increased, so are the overall wall-pressure levels on the suction side and the local levels around the edges on the pressure side.
2) The fast distortion of the turbulent fluctuations by the mean flow is at the origin of the changes in the pressure spectrum along the serration, following the estimated MS-T term presented in Fig. 11. Without loading, the amplitude of the pressure fluctuations decays progressing from the root to the tip (as also seen in [19]). This is a consequence of the wall-free condition in the gap region. On the suction side, a similar behaviour is observed. The higher incoming pressure fluctuations on the APG boundary layer are strongly dampened from the root to the tip of the serration.
3) The trailing vortices increase the shear along the edges. On the pressure side, vortex pairs interaction with the incoming fluctuations dominates the wall pressure. The streamlines deflection along the edges induces a spanwise eddy stretching and increases the pressure fluctuations across the edges. The vortex pairs also contribute to the pressure fluctuations along the suction side (Fig. 6) for highly loaded conditions.

Fig. 13 summarises the above conjecture about the stretching mechanisms induced by aerodynamic loading. The regions of increased pressure fluctuations (grey areas) and the direction of the distortion mechanism are represented in the figure. On the suction side, the higher wall-pressure fluctuations at the serration centre are associated with the streamwise stretching of the adverse pressure gradient boundary layer. On the pressure side, this occurs around the outer rim of the serrations, given the spanwise stretching imposed by the vortex pairs.
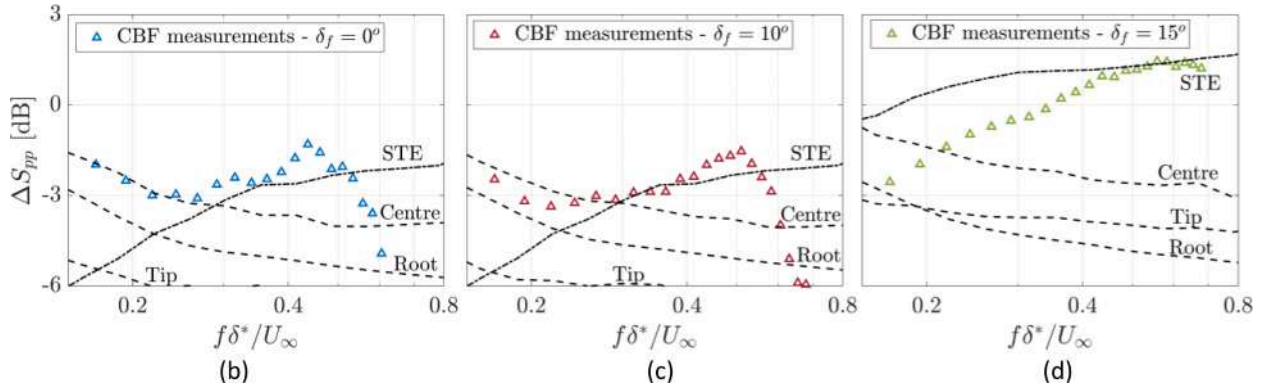
Fig. 14. Noise reduction with respect to measurements with a straight trailing edge observed for the serrated trailing edge at $\delta_f = 0°$, 10° and 15° (b, c, and d respectively). Negative values represent noise reduction. Predictions using Ayton's model using the pressure fluctuation levels at different regions along the serration edge are presented in black dashed lines. Doted dashed lines represent Ayton's prediction for the noise reduction considering a straight trailing edge with conditions equal to the serration tip.

Far-field noise prediction

The noise reduction achieved with the serrations with respect to the straight trailing edge is presented in Fig. 14a, b, and c. Along with the measurements, estimations for the noise reduction are performed with the model of Ayton [14]. The predictions are made in order to illustrate the impact that considering different distributions of the wall-pressure fluctuations has on the predicted noise reduction from trailing-edge serrations. The wall-pressure fluctuations measured at the root, centre, and tip of the serration are selected as input to the model. The model of Ayton requires the input of the incoming wall-pressure fluctuations, supposed uniform throughout the entire serration surface. By using a different input to the model, it is here considered that the entire serration surface will experience the levels of wall-pressure fluctuations of the root, centre, and tip respectively. Another curve, named STE, is proposed that considers all the scattered energy from the tip as if it would behave like a straight trailing edge (STE), is also reported. This curve follows the study of Avallone et al. [19] who conjectured that, at high frequency, the serrations scatter noise as a straight trailing edge with higher pressure fluctuations along the serration tip.

The maximum noise reduction measured is of about 3 dB and is captured at $f\delta^*/U_\infty \approx 0.25$ for 0°. As the flap angle is increased, this frequency is reduced. This Strouhal number is similar to that reported by Arce León et al. [7], and Avallone et al. [19]. In this frequency range, the wall-pressure levels are higher in the centre of the serration and, therefore, the scattered noise is dominated by the conditions at this region. This is indicated by the noise estimations using Ayton's method. Predictions using the wall pressure levels in the centre of the serration yield better comparisons with the measured noise reduction at low frequencies.

The predictions indicate that the low-frequency noise contributions, generated by turbulent structures larger or comparable to the serration wavelength, are not affected by the secondary flow and scatter noise following the conditions assumed in Ayton [9]. On the other hand, smaller flow structures (approximately $l_z < \lambda/6$, or $l_x < 2h/3$) are more affected by the secondary flow motions and depart from the assumptions of the frozen turbulence. The experimental data exhibit a good fit of the frequency where the maximum noise reduction is attained, according to eq. (8), provided that the smallest convection velocity from the two sides (suction side) is selected, which represents the smallest structures (lower u_c) for a chosen frequency.

$$f_{max} \approx 3.1 \frac{u_c}{2h} \tag{8}$$

For $f\delta^*/U_\infty > 0.25$, noise reduction is seen to decrease for all curves. The flow structures corresponding to this frequency range are significantly smaller in comparison to the serration dimensions and the highest scattering energy levels are quoted from the pressure side at the tip of the serration. The agreement with the analytical model in this frequency range is best for estimations given at the tip region but considering a straight trailing-edge geometry (STE curves in Fig. 14). Two aspects support the above hypothesis: first, the noise reduction is much poorer at the edges in comparison to the central region (slanted angle); furthermore, the small turbulent structures on the pressure side are more prone to the distortions imposed by the flow over the serration, resulting in a lower equivalent edge angle. The combined effect poses a limit for the noise reduction that can be obtained from serrations. This limit can be compared against the noise of a straight trailing edge with pressure fluctuations dominated by the levels at the serration tip. This assumption seems to produce accurate predictions up to $\delta_f \leq 10°$ and departs from them at $\delta_f = 15°$, where the low-frequency region exhibits noise reduction levels in between the sawtooth and the straight trailing-edge predictions. The discrepancies at such extreme angles can be linked to the more pronounced difference between the sawtooth and the straight trailing-edge estimations. The measured noise emissions lie in between the curves of the sawtooth and the straight trailing-edge prediction. The latter confirms that the assumption of frozen turbulence in a condition of strongly varying flow, such as in serrations under aerodynamic loading, leads to inaccurate noise predictions.

Conclusions

Measurements of the flow around a serrated trailing edge are studied to understand the effects of aerodynamic loading on the turbulent boundary layer trailing-edge noise reduction. A flat-plate model with a trailing-edge flap is used to control the aerodynamic loading condition. Time-resolved 3D-PIV measurements are complemented with non-intrusive surface pressure measurements to diagnose velocity and wall-pressure fluctuations over the serrations. Acoustic measurements with phased array technique complete the study with far-field predictions of the noise reduction.

The onset of streamwise vortices from approximately 25% of the serration height generates spanwise deflections that accelerate the flow towards the centre of the serration on the suction side and towards the gap region on the pressure side. The interaction of this secondary flow structure with the incoming turbulent flow from the boundary layer represents the major contribution to the increasing wall-pressure fluctuations along the serration. This effect is particularly strong on the pressure side, where the lower incoming fluctuations from the FPG flow are increased by the spanwise accelerations of the flow. The levels of the pressure fluctuations around the edges of the serration on the pressure side increase, with the maximum located around 60% of the sawtooth height. On the suction side, the vortex cores only impact the pressure fluctuations for highly loaded conditions. The variation of the wall-pressure spectrum over the serration surface is in the order of ± 4 dB and indicates that considering the amplitude of the wall-pressure fluctuations constant along the serration surface is not representative of the flow over trailing-edge serrations undergoing aerodynamic loading.

These results also reveal that noise estimations only based on the flow over the suction side might lead to inaccurate results. The suction side represents a critical region of low and mid-frequency noise, and results have shown that predictions based on the incoming turbulent boundary-layer conditions do not yield large deviations. Nevertheless, the flow alterations on the pressure side yield an increase in the noise levels at higher frequencies. The latter is dependent on the 3D characteristics of the flow and is a function of the flow angle and loading conditions, deviating increasingly from the predicted pressure fluctuations using the incoming boundary layer as the serration flap angle is increased.

The connection between the wall pressure and the velocity fluctuations at the vortex is analysed from the MS-T term, specifically at one boundary-layer momentum thickness above the serrations. The region of increased MS-T is driven by the acceleration of the stream and spanwise components of the flow velocity which, in combination with the increased velocity fluctuations, lead to the wall-pressure fluctuations captured along the serration edges.

Finally, acoustic measurements have shown the noise reduction provided by the serrated trailing edge under the different conditions tested. In agreement with the literature, noise reduction is maximum at about $f\delta^*/U_\infty = 0.25$ for no pressure gradient condition. This Strouhal number is shifted towards lower frequencies as the angle of the flap is increased and is bounded by the size of the coherent structures within the boundary layer in comparison to the serration geometry. Noise estimations using the model of Ayton [9] reveal that pressure conditions taken at the central part of the suction side of the serrations yield better comparisons with beamforming measurements at low to mid frequencies. At higher frequencies, noise reduction follows the predictions for an equivalent straight trailing edge. It is speculated that the small structures on the pressure side generate noise predominantly at the tip of the serration. The reduced scattering effectiveness of this portion of the serration bound the noise reduction achieved by the equivalent straight edge.

Lourenco Tercio Lima Pereira: Conceptualization, Methodology, Formal Analysis, Investigation, Writing – original draft, Writing – Review & Editing

Daniele Ragni: Conceptualization, Supervision, Writing – original draft, Writing – Review & Editing

Francesco Avallone: Conceptualization, Supervision, Writing – original draft, Writing – Review & Editing

Fulvio Scarano: Conceptualization, Supervision, Writing – original draft, Writing – Review & Editing

Declaration of Competing Interest

The authors declare that they have no known competing financial interests or personal relationships that could have appeared to influence the work reported in this paper.

Acknowledgments

Appendix A. – Pressure fluctuations and acoustic noise from the straight trailing-edge configuration

This appendix provides the analysis of the flow and noise characteristics measured for a straight trailing edge at 0 and 10° flap angle. The boundary-layer properties extracted for this case are used as normalising and scaling terms through the work and the acoustic measurements resulting from this configuration are used for the comparison of the noise against the sawtooth geometry presented in Section 4.4.

The mean flow over the trailing edge is presented in Fig. 15a and b. The boundary-layer profiles on both the suction and pressure side is given in Fig. 15c and d. The dashed lines in Fig. 15a and b represent the region of extraction of the boundary-layer quantities. The log and log-wake laws [34] are also included in the graph. Table 1 summarizes the relevant boundary-layer quantities measured
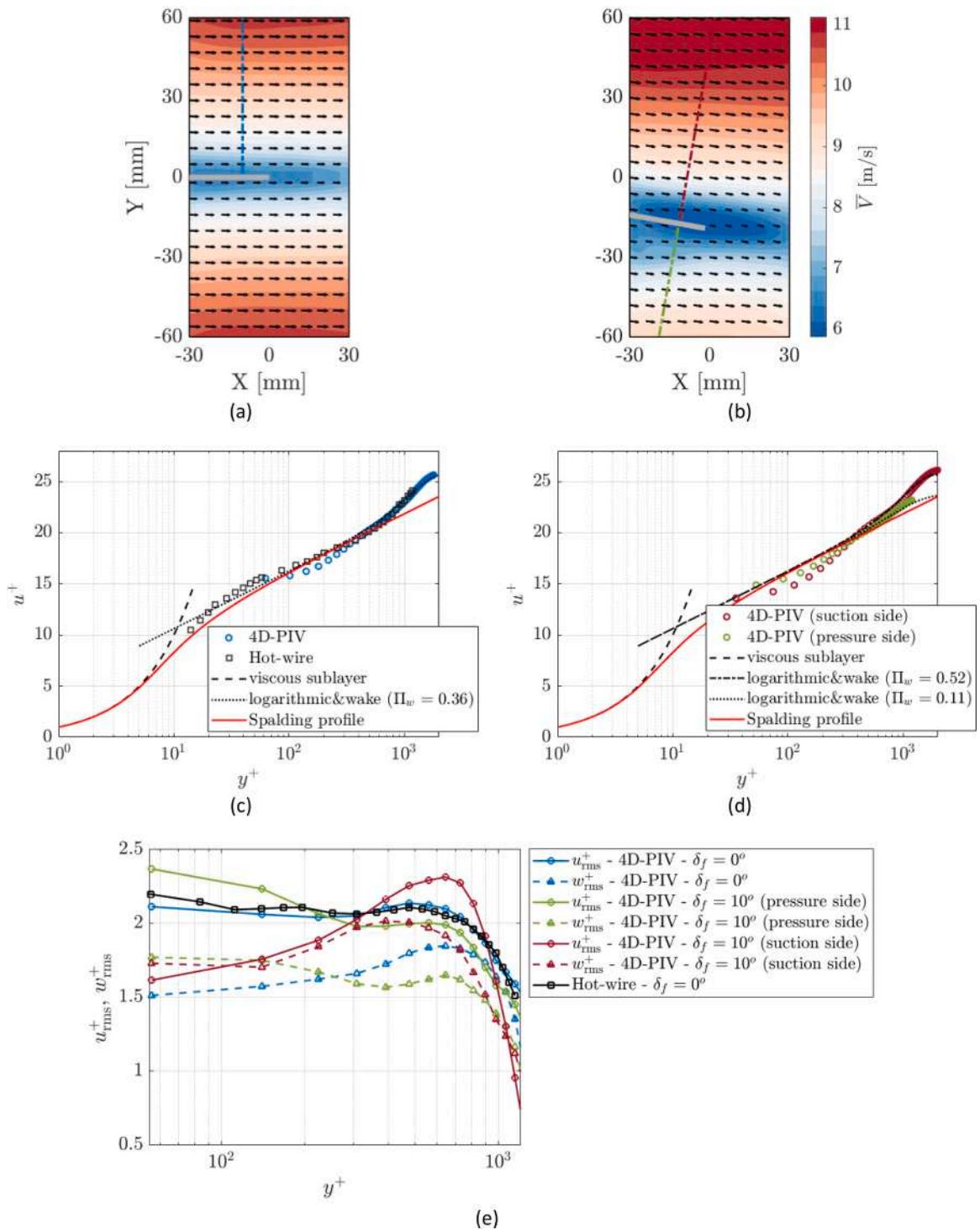
Fig. 15. Mean flow over the trailing edge and boundary-layer mean velocity profile measured at the trailing edge at $\delta_f = 0°$ (a and c respectively) and $\delta_f = 10°$ (b and d respectively) and root mean square (RMS) of the stream and spanwise velocity fluctuations (e). The dashed lines in (a) and (b) represent the region of extraction of the boundary-layer velocity profiles.

with the PIV technique. Fig. 15e shows the fluctuating velocity components. Fig. 15c, d, and e also demonstrate measurements with a hot-wire probe performed in the anechoic wind tunnel (A-tunnel) for comparisons against the PIV measurements. Discrepancies between the two measurements are below 0.8 m/s for the mean flow and 0.1 m/s for the root mean square velocity fluctuations, indicating that the characteristics of the incoming boundary layer are similar on both wind tunnels.

The pressure gradients are estimated from the variation of the edge velocity along the streamwise direction. Differently from airfoil measurements, where the angle of attack drastically changes the scales between pressure and suction side, at the flat plate the different pressure gradient conditions still yield similar boundary-layer heights. This contributes to the inspection of the different pressure gradient conditions over the loaded serrations as both pressure and suction sides have similar scales and, consequently, produce noise in a similar frequency range.

The wall-pressure spectrum measured with the surface-mounted microphones and the PIV technique is compared against the analytical models from Panton and Linebarger [40]; Goody [56]; Kamruzzaman [57] in Fig. 16. The Kamruzzaman model presented the best agreement with the current set of experimental data among the APG semi-empirical models. For the sake of conciseness, this is the only APG model presented here. The PIV measurements agree with the surface microphones with some underprediction observed at very low frequencies. Nevertheless, the model of Kamruzzaman overpredicts the outer and inner scales for the other conditions, especially for the FPG case. The Goody model overpredicts the frequency where the inner scale starts, what could be caused by the low Δ_* of the boundary layer formed in the flat plate.

The integral model from Panton can rather precisely predict the universal and starting of the inner scales. The model correctly identifies the pressure fluctuations for the ZPG and APG cases, with some over-prediction noted for the FPG one.

Fig. 16d and e show the variation of the spectrum in relation to the ZPG condition. Deviations from the methods are overall large. The increase in the wall-pressure spectrum on the suction side is highly under-predicted and even the results from the Panton model show a deviation in the order of 3 dB with respect to the measurements. Similarly, the pressure side is only mildly considered, and some pressure increase in the mid-frequencies, predicted by both Kamruzzaman and Panton models, is not captured during the experiments.
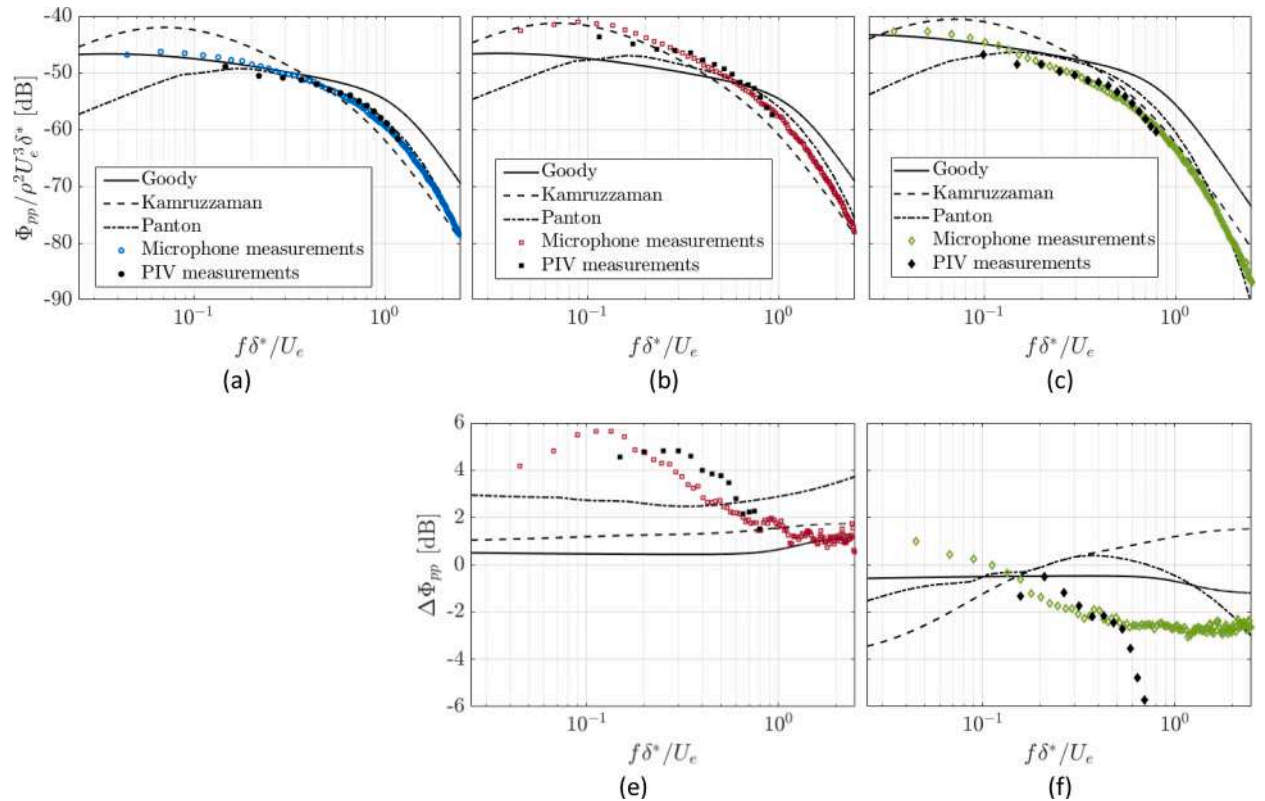

Fig. 16. Wall-pressure spectrum measured by the first pressure sensor of the trailing edge (M09) compared against PIV data and analytical models. Measurements are given at $\delta_f = 0°$ (a) and $\delta_f = 10°$ (suction and pressure side, b, and c respectively). Measured and estimated changes in the pressure spectrum with respect to the $\delta_f = 0°$ case are presented in (e) and (f).

In order to further analyse the spatial distribution of the wall-pressure structures, it is necessary to estimate the convective speed of such structures. Fig. 17 shows the convection velocity estimated from the microphone and PIV measurements at the trailing-edge sensors. This velocity is within the expected value of 60% of the free stream velocity [49] for the ZPG case. FPG conditions, given
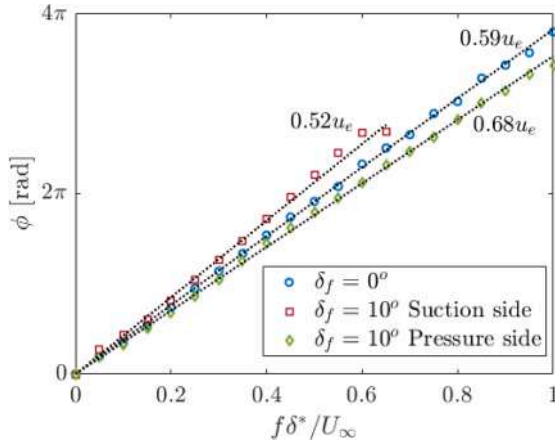
	Microphone	PIV
$\delta_f = 0^o$	6.0 m/s	6.1 m/s
$\delta_f = 10^o$ (suction)	5.8 m/s	6.0 m/s
$\delta_f = 10^o$ (pressure)	6.6 m/s	6.7 m/s

Fig. 17. Pressure fluctuations convection velocity estimated from the different angles of the straight trailing edge using the microphone and PIV measurements. In the graph, the markers represent the measured values and the dotted lines show the fitted expression used for the estimation of the convection velocity.

the higher associated velocity close to the wall, present an increased convection velocity (68% of the edge velocity, 6.6 m/s). On the suction side, the APG flow experiences a significant decrease in the same parameter (52% of the edge velocity, 5.8 m/s) induced by the smaller velocity gradient along the wall-normal direction at the wall. The table on the right-hand side of the graph compares the values obtained from the microphones and PIV measurements. The slightly higher value of the convection velocity estimated from the PIV measurements may be ascribed to the restrictions of the PIV technique, which limits the estimation within large structures that advect faster.

An estimation of the stream- and span-wise correlation length is presented in Fig. 18 with the microphone measurements. The fitting of the measured coherence between the sensors is plotted against the hypothesised exponential curve in Fig. 18a and b. The results demonstrate the quality of the fitting used for the estimation of the length of the coherent structures. Errors exist at the lowest frequencies, where the coherence levels are higher and the shape of the coherence distribution in space exits the exponential curve [23]. The resulting fitting of Corcos's equation with values by Hu and Herr [55] is also shown in the figure ($\alpha_x = 0.15$, and $\alpha_z = 0.71$). Following [55], the correlation length is seen to be well described as a function of the frequency and the convection velocity only. Predicting the convection velocity at such conditions is keen in obtaining a precise spatial description of the flow fluctuations near the trailing edge. Discrepancies with the model of Hu and Herr [55] are higher for the streamwise correlation length, where a better fit is obtained with a constant value $\alpha_x = 0.17$ instead of 0.15.

Predictions of the trailing-edge noise using the model described in Roger & Moreau (2005) [47] in the centre of the array location are presented in Fig. 19. The figure shows the measured wall pressure levels ($\Pi_{pp} = \phi_{pp} l_z$) combined from both sides of the model. The higher fluctuations on the suction side, even when combined with the lower convection speed, still make the suction side the dominant noise source for $\delta_f = 10°$ in low frequencies. At high frequencies, the $\delta_f = 0°$ and the $\delta_f = 10°$ have similar Π_{pp} and are expected to produce similar noise levels. Fig. 19b and c compare the measured far-field noise from the beamforming measurements against the predicted values. Differences in speed are corrected with a scaling of M^5. Results demonstrate the agreement between the experiment and scattering predictions. Overall, the noise is underestimated by the analytical method for the $\delta_f = 0°$ case, resulting in higher differences between the 0° and the 10° case. Higher errors are observed for low and high frequencies. This is caused by the acoustic measurement technique applied, which is limited at low frequencies due to the large beamwidth of the background sources and at high frequencies due to the contamination of the noise sources by spurious side lobes. Another explanation for the high-frequency bump observed in both cases is the possibility of a remaining shedding from the wake. This would agree with the Strouhal number based on the trailing-edge thickness ($St_t = 0.1$) despite the small thickness of the trailing edge in comparison to the boundary layer one ($t / \delta^* = 0.11$), following the criteria established in Blake [58].

The experiments with the straight trailing edge indicate that prediction of the trailing-edge scattering noise from measurements of the wall-pressure spectrum is reliable and can well identify the trends observed for different incoming boundary layers. The results support the comparisons made against the noise reduction of the serrated trailing edges, suggesting that major deviations with the
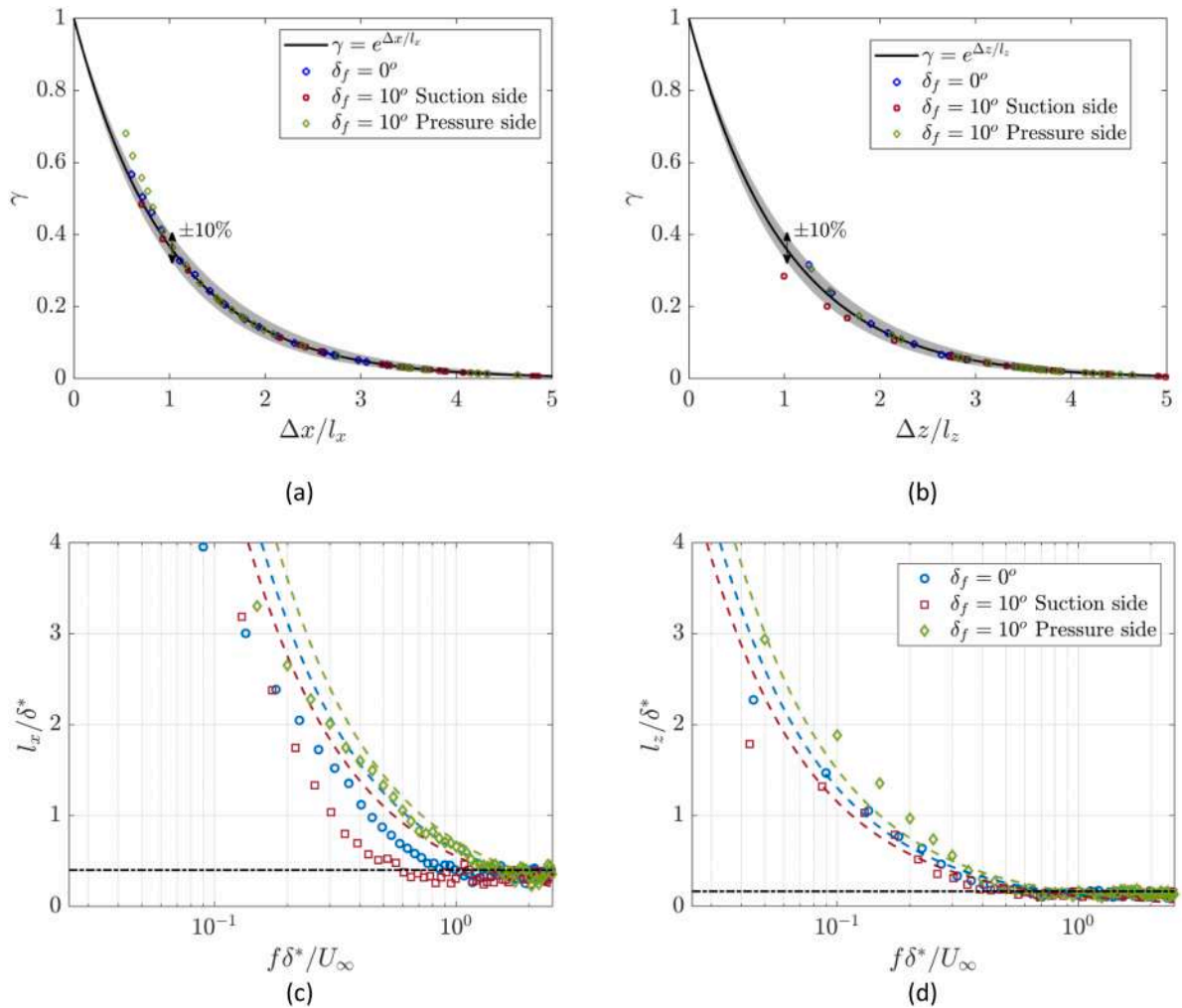
Fig. 18. Measured coherence levels between microphones compared against the proposed exponential coherence curve assumed for the estimation of the streamwise (a) and spanwise (b) correlation lengths. The computed streamwise and spanwise correlation lengths at $\delta_f = 0°$ and $\delta_f = 10°$ are shown in (c) and (d). The markers represent the measured values while the colored dashed curves show the fitting constants present in the work of Hu and Herr [55]. The black dot-dashed lines represent the limit of the measurement technique considering coherence levels below 0.05 for two adjacent microphone sensors.
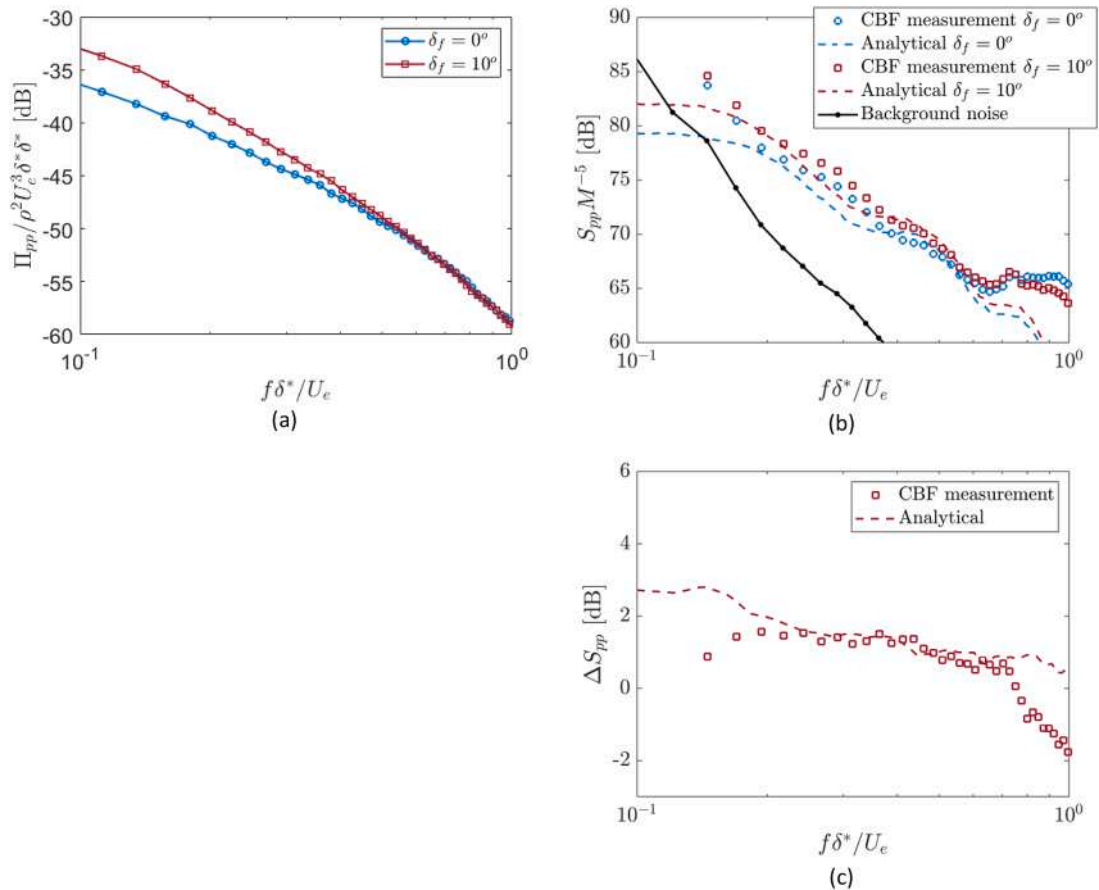
Fig. 19. Comparison between noise predicted and measured with Conventional beamforming (CBF) technique for $\delta_f = 0°$ and $\delta_f = 10°$. (a) shows the wall-pressure energy spectrum, (b) the far-field noise and (c) differences between the measurements at 10 and 0° ($\Delta S_{pp} = S_{pp}^{10} - S_{pp}^{0}$).

analytical comparisons are ascribed to the modelling of the serrated trailing edges and not to the description of the incoming flow conditions and reference straight trailing-edge noise.

References

[1] S. Oerlemans, P. Sijtsma, B.Méndez López, Location and quantification of noise sources on a wind turbine, J. Sound Vib. 299 (2007) 869–883, https://doi.org/10.1016/j.jsv.2006.07.032.

[2] J.E. Ffowcs-Williams, L.H. Hall, Aerodynamic sound generation by turbulent flow in the vicinity of a scattering half plane, J. Fluid Mech. 40 (1970) 657–670, https://doi.org/10.1017/S0022112070000368.

[3] M.S. Howe, Aerodynamic noise of a serrated trailing edge, J. Fluids Struct. 5 (1991) 33–45, https://doi.org/10.1016/0889-9746(91)80010-B.

[4] S. Lee, L. Ayton, F. Bertagnolio, S. Moreau, T. Pei, P. Joseph, Turbulent boundary layer trailing-edge noise : Theory, computation, experiment,and application, Prog. Aerosp. Sci. 126 (2021).

[5] S. Oerlemans, M. Fisher, T. Maeder, K. Kögler, Reduction of Wind Turbine Noise Using Optimized Airfoils and Trailing-Edge Serrations, AIAA J 47 (2009) 1470–1481, https://doi.org/10.2514/1.38888.

[6] M.S. Howe, Noise produced by a sawtooth trailing edge, J. Acoust. Soc. Am. 90 (1991) 482–487, https://doi.org/10.1121/1.401273.

[7] C. Arce León, D. Ragni, S. Pröbsting, F. Scarano, J. Madsen, Flow topology and acoustic emissions of trailing edge serrations at incidence, Exp. Fluids. (2016) 57, https://doi.org/10.1007/s00348-016-2181-1.

[8] M. Gruber, P. Joseph, T. Chong, On the mechanisms of serrated airfoil trailing edge noise reduction, in: 17th AIAA/CEAS Aeroacoustics Conf. (32nd AIAA Aeroacoustics Conf. (2011), 2022, pp. 5–8, https://doi.org/10.2514/6.2011-2781.

[9] L.J. Ayton, Analytic solution for aerodynamic noise generated by plates with spanwise-varying trailing edges, J. Fluid Mech. 849 (2018) 448–466, https://doi.org/10.1017/jfm.2018.431.

[10] B. Lyu, M. Azarpeyvand, S. Sinayoko, Prediction of noise from serrated trailing edges, J. Fluid Mech. 793 (2016) 556–588, https://doi.org/10.1017/jfm.2016.132.

[11] G.I. Taylor, The Spectrum of Turbulence, Proc. R. Soc. London. Ser. A - Math. Phys. Sci. 164 (1938) 476–490, https://doi.org/10.1098/rspa.1938.0032.

[12] R.H. Kraichnan, Pressure Fluctuations in Turbulent Flow over a Flat Plate, J. Acoust. Soc. Am. 28 (1956) 378–390, https://doi.org/10.1121/1.1908336.

[13] M. Sanjosé, S. Moreau, B. Lyu, L.J. Ayton, Analytical, numerical and experimental investigation of trailing-edge noise reduction on a Controlled Diffusion airfoil with serrations. 25th AIAA/CEAS Aeroacoustics Conf, 2019, https://doi.org/10.2514/6.2019-2450.

[14] B. Lyu, L.J. Ayton, Rapid noise prediction models for serrated leading and trailing edges, J. Sound Vib. 469 (2020), 115136, https://doi.org/10.1016/j.jsv.2019.115136.

[15] P. Kholodov, S. Moreau, Optimization of serrations for broadband trailing-edge noise reduction using an analytical model, (2019) 1–14, doi:10.2514/6.2019-2655.

[16] P. Kholodov, S. Moreau, Optimization of trailing-edge serrations with and without slits for broadband noise reduction, J. Sound Vib. 490 (2020), 115736, https://doi.org/10.1016/j.jsv.2020.115736.

[17] C. Arce León, R. Merino-Martínez, D. Ragni, F. Avallone, F. Scarano, S. Pröbsting, M. Snellen, D.G. Simons, J. Madsen, Effect of trailing edge serration-flow misalignment on airfoil noise emissions, J. Sound Vib. 405 (2017) 19–33, https://doi.org/10.1016/j.jsv.2017.05.035.

[18] T.P. Chong, A. Vathylakis, On the aeroacoustic and flow structures developed on a flat plate with a serrated sawtooth trailing edge, J. Sound Vib. 354 (2015) 65–90, https://doi.org/10.1016/j.jsv.2015.05.019.

[19] F. Avallone, W.C.P. van der Velden, D. Ragni, D. Casalino, Noise reduction mechanisms of sawtooth and combed-sawtooth trailing-edge serrations, J. Fluid Mech. 848 (2018) 560–591, https://doi.org/10.1017/jfm.2018.377.

[20] L.E. Jones, R.D. Sandberg, Acoustic and hydrodynamic analysis of the flow around an aerofoil with trailing-edge serrations, J. Fluid Mech. 706 (2012) 295–322, https://doi.org/10.1017/jfm.2012.254.

[21] D. Ragni, F. Avallone, W.C.P. van der Velden, D. Casalino, Measurements of near-wall pressure fluctuations for trailing-edge serrations and slits, Exp. Fluids. 60 (6) (2019), https://doi.org/10.1007/s00348-018-2654-5.

[22] G. Romani, D. Casalino, W. van der Velden, Numerical analysis of airfoil trailing-edge noise for straight and serrated edges at incidence, AIAA J 59 (2021) 2558–2577, https://doi.org/10.2514/1.J059457.

[23] S. Pröbsting, M. Tuinstra, F. Scarano, Trailing edge noise estimation by tomographic Particle Image Velocimetry, J. Sound Vib. 346 (2015) 117–138, https://doi.org/10.1016/j.jsv.2015.02.018.

[24] D.J. Moreau, C.J. Doolan, Noise-Reduction Mechanism of a Flat-Plate Serrated Trailing Edge, AIAA J 51 (2013) 2513–2522, https://doi.org/10.2514/1.j052436.

[25] M.P.J. Sanders, L.D. De Santana, M. Azarpeyvand, C.H. Venner, Unsteady surface pressure measurements on trailing edge serrations based on digital MEMS microphones, 2018 AIAA/CEAS Aeroacoustics Conf (2018) 1–12, https://doi.org/10.2514/6.2018-3290.

[26] F. Scarano, S. Ghaemi, G.C.A. Caridi, J. Bosbach, U. Dierksheide, A. Sciacchitano, On the use of helium-filled soap bubbles for large-scale tomographic PIV in wind tunnel experiments, Exp. Fluids. (2015) 56, https://doi.org/10.1007/s00348-015-1909-7.

[27] D. Schanz, S. Gesemann, A. Schröder, Shake-The-Box: Lagrangian particle tracking at high particle image densities, Exp. Fluids. 57 (2016) 1–27, https://doi.org/10.1007/s00348-016-2157-1.

[28] J.F.G. Schneiders, F. Scarano, Dense velocity reconstruction from tomographic PTV with material derivatives, Exp. Fluids. 57 (2016) 1–22, https://doi.org/10.1007/s00348-016-2225-6.

[29] L.T. Lima Pereira, D. Ragni, F. Avallone, F. Scarano, Pressure fluctuations from large-scale PIV over a serrated trailing edge, Exp. Fluids. 61 (2020) 1–17, https://doi.org/10.1007/s00348-020-2888-x.

[30] R. Merino-Martínez, A. Rubio Carpio, L.T. Lima Pereira, S. van Herk, F. Avallone, D. Ragni, M. Kotsonis, Aeroacoustic design and characterization of the 3D-printed, open-jet, anechoic wind tunnel of Delft University of Technology, Appl. Acoust. (2020) 170, https://doi.org/10.1016/j.apacoust.2020.107504.

[31] E. Rodríguez-López, P.J.K. Bruce, O.R.H. Buxton, On the Formation Mechanisms of Artificially Generated High Reynolds Number Turbulent Boundary Layers, Boundary-Layer Meteorol 160 (2016) 201–224, https://doi.org/10.1007/s10546-016-0139-8.

[32] W.K. Blake, Essentials of Turbulent Wall Pressure Fluctuations, 2017, doi:10.1016/b978-0-12-809274-3.00002-7.

[33] F.H. Clauser, The Turbulent Boundary Layer, Adv. Appl. Mech. 4 (1956) 1–51, https://doi.org/10.1016/S0065-2156(08)70370-3.

[34] D. Coles, The law of the wake in the turbulent boundary layer, J. Fluid Mech. 1 (1956) 191–226, https://doi.org/10.1017/S0022112056000135.

[35] P.R. Spalart, J.H. Watmuff, Experimental and numerical study of a turbulent boundary layer with pressure gradients, J. Fluid Mech. 249 (1993) 337, https://doi.org/10.1017/S002211209300120X.

[36] T.F. Brooks, M.A. Marcolini, D.S. Pope, Airfoil Trailing Edge Flow Measurements and Comparisons With Theory, Incorporating Open Wind Tunnel Corrections, AIAA Pap, 1984, https://doi.org/10.2514/6.1984-2266.

[37] D.E. Faleiros, M. Tuinstra, A. Sciacchitano, F. Scarano, Helium-filled soap bubbles tracing fidelity in wall-bounded turbulence, Exp. Fluids. 59 (2018) 1–13, https://doi.org/10.1007/s00348-018-2502-7.

[38] S. Ghaemi, D. Ragni, F. Scarano, PIV-based pressure fluctuations in the turbulent boundary layer, Exp. Fluids. 53 (2012) 1823–1840, https://doi.org/10.1007/s00348-012-1391-4.

[39] K. Lynch, F. Scarano, A high-order time-accurate interrogation method for time-resolved PIV, Meas. Sci. Technol. (2013) 24, https://doi.org/10.1088/0957-0233/24/3/035305.

[40] R.L. Panton, J.H. Linebarger, Wall pressure spectra calculations for equilibrium boundary layers, J. Fluid Mech. 65 (1974) 261–287, https://doi.org/10.1017/S0022112074001388.

[41] G.P. Romano, Analysis of two-point velocity measurements in near-wall flows, Exp. Fluids. 20 (1995) 68–83, https://doi.org/10.1007/BF00189296.

[42] S. Luesutthiviboon, A. Malgoezar, M. Snellen, P. Sijtsma, D. Simons, Improving source discrimination performance by using an optimized acoustic array and adaptive high-resolution CLEAN-SC beamforming, in: 7th Berlin Beamforming Conf., 2018, pp. 1–26.

[43] P. Sijtsma, Phased Array Beamforming Applied to Wind Tunnel and Fly-Over Tests, in: SAE Tech. Pap. 2010–Octob, 2010, pp. 17–19, https://doi.org/10.4271/2010-36-0514.

[44] E. Sarradj, Three-dimensional acoustic source mapping with different beamforming steering vector formulations, Adv. Acoust. Vib. (2012) 2012, https://doi.org/10.1155/2012/292695.

[45] T.F. Brooks, W.M. Humphreys, Effect of directional array size on the measurement of airframe noise components, in: 5th AIAA/CEAS Aeroacoustics Conf. Exhib, 1999, https://doi.org/10.2514/6.1999-1958.

[46] R.K. Amiet, Noise due to turbulent flow past a trailing edge, J. Sound Vib. 47 (1976) 387–393, https://doi.org/10.1016/0022-460X(76)90948-2.

[47] M. Roger, S. Moreau, Back-scattering correction and further extensions of Amiet's trailing-edge noise model. Part 1: Theory, J. Sound Vib. 286 (2005) 477–506, https://doi.org/10.1016/j.jsv.2004.10.054.

[48] R.K. Amiet, High frequency thin-airfoil theory for subsonic flow, AIAA J 14 (1976) 1076–1082, https://doi.org/10.2514/3.7187.

[49] G.M. Corcos, The structure of the turbulent pressure field in boundary-layer flows, J. Fluid Mech. 18 (1964) 353–375.

[50] G.M. Corcos, Resolution of Pressure in Turbulence, J. Acoust. Soc. Am. 35 (1963) 192–199, https://doi.org/10.1121/1.1918431.

[51] G.M. Lilley, T.H. Hodgson, On surface pressure fluctuations in turbulent boundary layers, Advis. Gr. Aeronaut. Res. Dev. Paris. Report 276 (1960).

[52] P. Jaiswal, S. Moreau, F. Avallone, D. Ragni, S. Pröbsting, On the use of two-point velocity correlation in wall-pressure models for turbulent flow past a trailing edge under adverse pressure gradient, Phys. Fluids. 32 (2020), 105105, https://doi.org/10.1063/5.0021121.

[53] F. Avallone, S. Pröbsting, D. Ragni, Three-dimensional flow field over a trailing-edge serration and implications on broadband noise, Phys. Fluids. (2016) 28, https://doi.org/10.1063/1.4966633.

[54] F. Avallone, W.C.P. van der Velden, D. Ragni, Benefits of curved serrations on broadband trailing-edge noise reduction, J. Sound Vib. 400 (2017) 167–177, https://doi.org/10.1016/j.jsv.2017.04.007.

[55] N. Hu, M. Herr, Characteristics of wall pressure fluctuations for a flat plate turbulent boundary layer with pressure gradients, in: 22nd AIAA/CEAS Aeroacoustics Conf. 2016, 2016, pp. 1–18, https://doi.org/10.2514/6.2016-2749.

[56] M. Goody, Empirical Spectral Model of Surface Pressure Fluctuations, AIAA J 42 (2008) 1788–1794, https://doi.org/10.2514/1.9433.

[57] M. Kamruzzaman, D. Bekiropoulos, T. Lutz, W. Würz, E. Krämer, A Semi-Empirical Surface Pressure Spectrum Model for Airfoil Trailing-Edge Noise Prediction, Int. J. Aeroacoustics. 14 (2015) 833–882, https://doi.org/10.1260/1475-472x.14.5-6.833.

[58] W.K. Blake, Noncavitating Lifting Sections, 2017, doi:10.1016/b978-0-12-809274-3.00005-2.